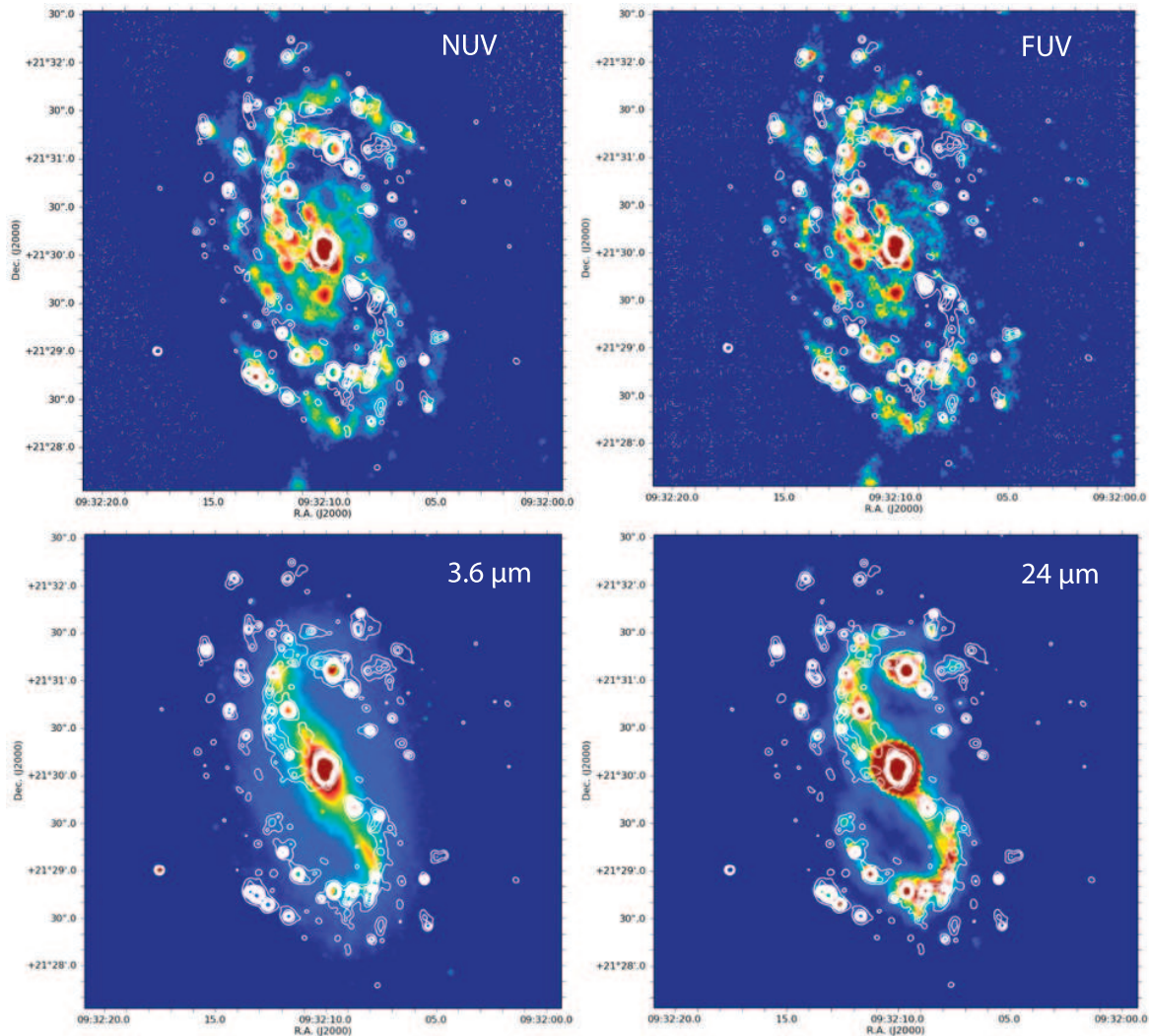


# A comprehensive study of the star-formation along the strong NGC 2903 bar

A study from the far-ultraviolet to the radio



*H $\alpha$  contours on morphologically complex barred spiral NGC 2903*

G. Popping<sup>1</sup>

Supervisors: I. Pérez<sup>2,3</sup>, J.M. van der Hulst<sup>1</sup>, A. Zurita<sup>2,3</sup>

July 9, 2010

---

<sup>1</sup>Kapteyn Astronomical Institute, University of Groningen

<sup>2</sup>Dep. Física Teórica y del Cosmos, Universidad de Granada

<sup>3</sup>Instituto Carlos I de Física Teórica y Computación, Spain



---

# Contents

<b>1</b>	<b>Introduction</b>	<b>1</b>
<b>2</b>	<b>Multiwavelength study of the star-formation in the bar of NGC 2903</b>	<b>3</b>
2.1	Introduction . . . . .	3
2.2	Observations and data reduction . . . . .	5
2.2.1	H $\alpha$ imaging . . . . .	5
2.2.2	<i>Spitzer</i> Infrared images . . . . .	7
2.2.3	<i>GALEX</i> images . . . . .	8
2.2.4	Other data: ground-based optical images and CO ( $J=1-0$ ) . . . . .	8
2.3	The general morphology of NGC 2903 . . . . .	8
2.4	Photometry of star-forming regions . . . . .	10
2.4.1	HII region catalogue . . . . .	10
2.4.2	UV photometry . . . . .	12
2.4.3	Dust attenuation . . . . .	14
2.5	Results . . . . .	18
2.5.1	H $\alpha$ luminosity and $EW_{H\alpha}$ . . . . .	18
2.5.2	Dust attenuation . . . . .	19
2.5.3	Star-formation rate . . . . .	19
2.5.4	UV colours and cluster ages . . . . .	20
2.6	Discussion . . . . .	24
2.7	Summary and conclusions . . . . .	26
<b>3</b>	<b>Links between star-formation and H I and H<math>\alpha</math> gas kinematics in NGC 2903</b>	<b>29</b>
3.1	Introduction . . . . .	30
3.2	Data . . . . .	31
3.2.1	H I data cube . . . . .	31

---

3.2.2	H $\alpha$ data cube . . . . .	32
3.3	H I map and kinematics . . . . .	33
3.3.1	General H I features . . . . .	33
3.3.2	Velocity field . . . . .	34
3.3.3	Rotation curve . . . . .	34
3.3.4	H I model velocity field and non-circular velocity maps . . . . .	39
3.4	H $\alpha$ kinematics . . . . .	41
3.4.1	H $\alpha$ velocity field . . . . .	41
3.4.2	Ionised gas non-circular motions . . . . .	42
3.4.3	H $\alpha$ velocity gradients . . . . .	47
3.5	Discussion . . . . .	48
3.6	Summary and Conclusion . . . . .	50
<b>4</b>	<b>Conclusion and future work</b>	<b>53</b>
<b>5</b>	<b>Acknowledgements</b>	<b>55</b>
	<b>Bibliography</b>	<b>57</b>

---

## Introduction

The presence of a bar is known to be an efficient mechanism to redistribute angular momentum and matter in galaxies up to large distances. Because of this ability, bars are considered to play an important role in the evolution of disk galaxies. Inflow of gas through the bar towards the galaxy central part is provoked by the loss of angular momentum, due to the bar gravity torque. This inflow of gas is believed to fuel the central black hole (e.g., Shlosman et al. 1989).

Within the local Universe, ~60% of the spiral galaxies contain a bar (e.g., Knapen et al. 2000, Eskridge et al. 2000; Menéndez-Delmestre et al. 2007; Marinova & Jogee 2007, Hernández-Toledo 2007). Despite their frequency and important role in the secular evolution of spiral galaxies, their origin and evolution is not well known yet.

A detailed study of the star-formation history in bars linked to the galaxy dynamics, can help to understand how bars form and evolve. It was commonly believed that the presence and absence of star-formation along bars is determined by the bar strength. Hydrodynamical simulations pointed out that strong shocks and high shear in strong bars prevent the collapse of molecular clouds (e.g., Athanassoula 1992, 2000). This led to the statement that star-formation does not occur within bars of strongly-barred galaxies (e.g., NGC 5248; Jogee et al. 2002). However, there are several examples of strongly barred spirals with star-formation along their bar (e.g., NGC 7749, NGC 613, NGC 1097, NGC 1530, NGC 2903). Although star-formation is inhibited or suppressed by strong shear, some strongly-barred galaxies do contain H II regions at other locations in their bar structure (e.g., Martin & Friedli 1997; Sheth et al. 2002). This gives rise to the question of what determines the presence or absence of star-forming regions along strong bars. Knowledge of both the recent star-formation history of the bar and the underlying dynamical behaviour of the gas allows us to address this question.

Strong bars containing star-formation along their bar structure are also excellent places to study the physical parameters that trigger and inhibit star-formation in general. The presence of strong shocks, shear, non-circular motions (Pence & Blackman 1984; Athanassoula 1992; Reynaud & Downes 1998; Zurita et al. 2004) and strong magnetic-fields (Beck 2002) provide perfect conditions to achieve understanding on how these factors affect star-formation.

The aim of this study is to determine the recent star-formation history of the strongly barred spiral NGC 2903 (bar strength of 3; Laurikainen & Salo 2002) and to relate it to the bar/galaxy dynamics. NGC 2903 is close by (8.9 Mpc; Drozdovsky & Karachentsev 2000) and a typical example of a strong bar with star-formation along its bar (Sheth et al. 2002). Although the NGC

2903 bar can not be considered amongst the strongest observed, star-formation along the bar and its distance make the galaxy an ideal object to study the effects that trigger star-formation along strong bars.

This report describes two different projects. In the first, we extensively study the current and recent star-formation of NGC 2903 using a wavelength regime running from the far-ultraviolet to the sub-millimeter, and relate this to the bar morphological features. In the second project, we present the kinematics of the neutral and ionised gas in NGC 2903. We investigate the relation between the gas kinematics and star-formation in the bar. We end with a summary, conclusion and future work.

---

# Multiwavelength study of the star-formation in the bar of NGC 2903

– G. Popping, I Pérez & A. Zurita –

*Based on: Popping et al. (2010), accepted for publication in "Astronomy & Astrophysics"*

## Abstract

*The nearby barred spiral NGC 2903 has an active starburst at its centre and H $\alpha$  regions distributed along its bar. We analyse the star-formation properties in the bar region of NGC 2903 and study its links to the typical bar morphological features.*

*We combine space and ground-based data from the far-ultraviolet to the sub-millimeter spectral ranges to create a panchromatic view of the NGC 2903 bar. We produce two catalogues: one for the current star-formation regions, as traced by the H $\alpha$  compact emission, and a second for the ultraviolet (UV) emitting knots, containing positions and luminosities. From them, we obtain ultraviolet colours, star-formation rates, dust attenuation, and H $\alpha$  EWs, and analyse their spatial distribution. We estimate stellar cluster ages using stellar population synthesis models (Starburst99).*

*We find NGC 2903 to be a complex galaxy that has a very different morphology in each spectral band. The CO ( $J=1-0$ ) and the 3.6  $\mu\text{m}$  emission trace each other in a clear barred structure, while the H $\alpha$  leads both components and has an s-shape distribution. The UV emission is patchy and does not resemble a bar. The UV emission is also characterised by a number of regions located symmetrically with respect to the galaxy centre, almost perpendicular to the bar, in a spiral shape covering the inner  $\sim 2.5\text{kpc}$ . These regions exhibit a significant amount of neither H $\alpha$  nor 24  $\mu\text{m}$  emission. We estimate ages for these regions ranging from 150 to 320 Myr, older than the remaining UV knots, which have ages lower than 10 Myr. The SFR calculated from the UV emission is  $\sim 0.4 M_{\odot} \text{ yr}^{-1}$ , compatible with the SFR derived from H $\alpha$  calibrations ( $\sim 1 M_{\odot} \text{ yr}^{-1}$ ).*

## 2.1 Introduction

Following the launch of both the *Spitzer Space Telescope* and the *Galaxy Evolution Explorer (GALEX)*, knowledge about the star-formation (SF) in galaxies has grown considerably. The

panchromatic view of nearby galaxies offered by large surveys carried out by these space telescope missions have provided extraordinary databases with which to study star-formation in galaxies. In particular, it has allowed us to link general galaxy properties to those of the local interstellar medium (ISM) properties and the galaxy dynamics. Identifying these links is crucial for understanding SF in galaxies. In nearby galaxies, these sets of multiwavelength data provide an opportunity to study in detail, with good spatial resolution, the location and properties of relatively young populations, recent massive star-formation, and dust attenuation (e.g., Calzetti et al. 2005; Tamura et al. 2009; Relaño & Kennicutt 2009).

New dust and SF indicators have been developed and calibrated using all the available bands. The combination of  $24\ \mu\text{m}$  and  $\text{H}\alpha$  emission has become a reliable indicator of dust attenuation (Kennicutt et al. 2007; Relaño & Kennicutt 2009). Both bands are linked to star-formation processes, with the  $\text{H}\alpha$  emission originating from the recombination of hydrogen in the surrounding medium of very recently formed (less than a few Myr) massive stars, and the  $24\ \mu\text{m}$  emission tracing local star-formation radiation obscured by dust (Calzetti et al. 2005). Extinction-corrected UV emission can also be used to retrieve the star-formation rate (SFR) (Kennicutt 1998) and to obtain some insight into the star-formation that has occurred in the past Gyr (e.g., Bianchi et al. 2005; Hibbard et al. 2005). A combination of UV,  $\text{H}\alpha$ , and  $24\ \mu\text{m}$  emission is indeed ideal for reconstructing the recent star-formation history of a galaxy by studying the location and properties of individual clusters and those of the gas and dust emission around them. To date, and to our knowledge, only a few galaxies have been analysed in this way; M51 (Calzetti et al. 2005), M81 (Pérez-González et al. 2006), M33 (Relaño & Kennicutt 2009; Verley et al. 2009), and NGC 7331 (Thilker et al. 2007). Barred galaxies offer a useful tool for investigating the physical conditions that support star-formation in galaxies. The motions in bars are characterised by non-circular motions that push the gas into intersecting orbits, where shocks and star-formation can be triggered. The position and strength of the shocks are determined by the bar potential, the global dynamics within the bar region being driven by the bar. We now have a relatively good understanding of the gas behaviour under a bar potential (e.g., Pérez et al. 2004) and this knowledge can be used to understand the conditions triggering star-formation. Bars and their surroundings host extreme physical conditions and a variety of ISM environments. They are perfect places to study the link between the conditions favouring star-formation and the galaxy dynamics. Therefore, a panchromatic view revealing the history of star-formation in bars can provide a unique insight into the links between star-formation and the galaxy dynamics, which

**Table 2.1:** *Log of ground-based  $\text{H}\alpha$  observations.*

Band	Date	Filter	Exp. Time	Seeing
$\text{H}\alpha$	29 Oct 2007	WFCH6568	3x1200s	1.4''
R	30 Oct 2007	HARRIS R	3x250s	2.1''

may also help us to understand how bars form and evolve.

We present a detailed multiwavelength study of the star-formation in the bar region of NGC 2903 performed by analysing the correlations between the location and ages of the *young* stellar clusters, and the morphology of the bar. This was achieved in turn by analysing the emission in  $H\alpha$ , UV, and  $24\ \mu\text{m}$  as well as the optical data from the Sloan Digital Sky Survey (SDSS), in addition to  $8\ \mu\text{m}$  and CO (J=1-0) emission.

We have chosen NGC 2903 for this research for a number of reasons: it is close-by (8.9 Mpc; Drozdovsky & Karachentsev 2000) allowing us to achieve high spatial resolution ( $\sim 43\ \text{pc arcsec}^{-1}$ ), and is isolated from large companions, preventing major merger effects in the results. Irwin et al. (2009) studied the H I content of NGC 2903 demonstrating that it possesses a large H I envelope of around three times its optical size. They also found a small H I companion 64 kpc away from the galaxy in projection, which adds to a previously known small stellar companion. No clear sign of an interaction has been found so far.

NGC 2903 is an SBd galaxy showing a symmetric strong bar considered typical of this class of galaxies (Laurikainen & Salo 2002). Previous observations have shown large amounts of  $H\alpha$  emission along the bar and not only at the ends of the bar and nuclear region (Sheth et al. 2002). The CO (J=1 - 0), *Spitzer*, and *GALEX* data available makes this galaxy an ideal target for multiwavelength studies to retrieve insight into the star-formation history of bars.

A previous study by Leon et al. (2008) of the NGC 2903 bar showed that HCN(1-0) is distributed along the bar and at its centre. They compared the star-formation rate ratio of the bar to the centre with the predictions of numerical simulations by Martin & Friedli (1997). This made them propose that the bar in NGC 2903 has an age between 200 and 600 Myr.

The outline of the paper is as follows. In Sec. 2.2, we present the observational data and in Sec. 2.3 we analyse the general morphology of NGC 2903. We present our methodology to obtain the bar H II regions and UV emission knots catalogues in Sec. 2.4. The following section contains the main results regarding the  $EW_{H\alpha}$ , star-formation rates, UV colours, and ages of the stellar clusters. In Sec. 2.6, we discuss our main results and finally present a summary and conclusions.

## 2.2 Observations and data reduction

### 2.2.1 $H\alpha$ imaging

The  $H\alpha$  data of NGC 2903 was obtained with the Wide Field Camera at the 2.5m Isaac Newton Telescope at the Roque de los Muchachos Observatory in October 2007. A summary of the observations is presented in Table 1. The galaxy was observed through a  $95\ \text{\AA}$  width narrow-band filter with a total exposure time of 3600s, and an R-band filter, used for the continuum subtraction, with an exposure time of 750s. We carried out the overscan subtraction, bias, and

flatfield correction using standard reduction tasks within IRAF<sup>1</sup>. The sky subtraction was carried out by fitting a first order polynomial to a sky map created using the mean sky values derived from several positions on the image, free of both foreground stars and galaxy emission. The H $\alpha$ +continuum and R-band images were then aligned using the positions of field stars in the images and combined separately to produce the final images. Before continuum subtraction the, H $\alpha$ +continuum image was degraded to the resolution of the R-band image ( $\sim 2.1$  arcsec).

The continuum subtraction was done as described by Relaño et al. (2005). We used 11 non-saturated foreground stars in both the H $\alpha$  (ON-band) and in the continuum R-band (OFF-band) images. The fluxes of these stars yielded a mean flux ratio ON-band/OFF-band of  $0.34 \pm 0.02$ . This value was then used as a starting point scaling factor to generate a set of OFF-band images scaled with factors ranging from 0.32 to 0.36. These images were afterwards subtracted from the ON-band image to produce images free of continuum emission. After a close inspection of the resulting images, we adopted a value of  $0.34 \pm 0.01$  for the continuum scaling factor. The uncertainty in the continuum scaling factor produces differences of up to  $\sim 3\%$  in the integrated fluxes of the H II regions.

The astrometry of the H $\alpha$  image was performed using the USNO2 catalogue coordinates for the foreground stars of the galaxy images, resulting in an accuracy of  $\sim 0.39''$ . The observations were made during non-photometric conditions. Therefore, for the flux calibration, we used previously reported fluxes of 11 H II regions located in the disk of NGC 2903 published by (Mayya 1994). We compared the flux reported there with our measured flux (in ADU) using identical apertures. We then calculated the ratio for each region and assumed the median to be our final H $\alpha$  flux calibration factor ( $(2.2 \pm 0.4) \times 10^{-19} \text{ erg s}^{-1} \text{ cm}^{-2} \text{ count}^{-1}$ ). The error was calculated by taking the standard deviation of the flux ratio for all the stars. The scaling relation is presented in Fig. 2.1. The  $2\sigma$  sensitivity limit of the final H $\alpha$  image is  $6.2 \times 10^{-17} \text{ erg s}^{-1} \text{ cm}^{-2}$  per pixel.

The H $\alpha$  data of Mayya et al. (1994) from which our fluxes were flux calibrated were not corrected for Galactic extinction. Therefore, the H II region luminosities of our catalogued H II regions were corrected *a posteriori* for foreground Galactic extinction (Schlegel et al. 1998), which was assumed to be  $A_{H\alpha} = 0.08$  mag.

The bandwidth of the H $\alpha$  filter can also be affected by emission from the [N II] $\lambda 6548\text{\AA}$  and [N II] $\lambda 6584\text{\AA}$  emission lines at their corresponding redshifted wavelengths. A proper correction for this requires spectroscopic information about all the H II regions, which information is not currently available. The typical [N II]/H $\alpha$  ratio for extragalactic H II regions of solar metallicity is approximately 0.33 (e.g., Kennicutt & Kent 1983). Therefore, an approximate correction of 25% should be applied to the H $\alpha$  fluxes and equivalent widths. Rather than applying this average correction to the fluxes of all H II regions, we decided to present the uncorrected H $\alpha$ + [N II]

---

<sup>1</sup>IRAF is distributed by the National Optical Astronomy Observatories, which is operated by the Association of Universities for Research in Astronomy, Inc. (AURA) under cooperative agreement with the National Science Foundation.

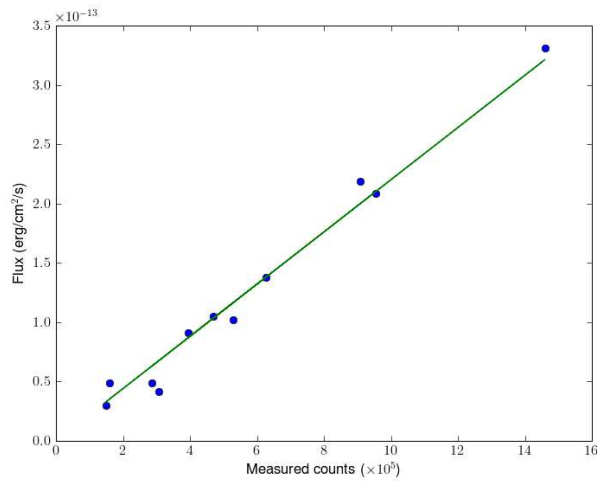


**Figure 2.1:** Scaling relation from our measured  $H\alpha+[NII]$  fluxes in counts to earlier measurements made by Mayya et al. (1994) for the same  $HII$  regions. The  $HII$  region fluxes measured by Mayya et al. (1994) also contain  $[NII]$  emission.

luminosities in Table 2.

### 2.2.2 *Spitzer* Infrared images

To investigate the extinction and the star-formation in the bar of NGC 2903 we used the *Spitzer* 24  $\mu\text{m}$  observations from the Multiband Imaging Photometer (MIPS) instrument (Werner et al. 2004; Fazio et al. 2004; Rieke et al. 2004). The data was obtained in April 2004 as part of the Local Volume Legacy Survey (Lee et al. 2008; Kennicutt et al. 2007). MIPS reduction steps are described in detail by Gordon et al. (2005). The field of view covered by the observations is large enough to contain the whole galaxy with enough sky coverage allowing a good sky subtraction. The 24  $\mu\text{m}$  point-spread function (PSF) has a measured FWHM of  $\sim 5.6''$  and a  $2\sigma$  sensitivity limit of  $0.52 \times 10^{-6} \text{ Jy arcsec}^{-2}$ . The image was registered to the same coordinate system and pixel scale as the  $H\alpha$  image and the background was subtracted in the same way as for the  $H\alpha$  image.

The 24  $\mu\text{m}$  image has a much larger PSF FWHM than the  $H\alpha$  image (FWHM  $\sim 2.1''$ ). Therefore, to allow for accurate comparisons, we produced a convolved version of the  $H\alpha$  image corresponding to the 24  $\mu\text{m}$  PSF by applying a PSF kernel as described by Gordon et al. (2008). This version of the image was only used to calculate the  $H\alpha$  attenuation of the  $HII$  regions (Sec. 2.4.3). As complementary data, we also used the 3.6 and 8  $\mu\text{m}$  images, which have a PSF FWHM  $\sim 2''$  in both bands. These images were only used to carry out global morphological comparisons with the remaining bands; we therefore registered the images to the same coordinate system as the  $H\alpha$  image, but we did not degrade their spatial resolution.

### 2.2.3 GALEX images

To analyse the UV emission and its distribution in NGC 2903, we used *GALEX* mission data (Martin et al. 2005). The *GALEX* direct imaging observations were centered on 1529Å and 2312Å for the far-ultraviolet (FUV, 1350 - 1750Å) and near-ultraviolet (NUV, 1750-2750Å) bands, respectively. NGC 2903 was observed in February 2004 as part of the *Nearby Galaxies Survey* (NGS, Bianchi et al. 2003) with an exposure time of 1862s and 1861s for the FUV and NUV, respectively. The PSF FWHM of the images are  $\sim 4.2$  and  $\sim 4.6''$  for the FUV and NUV, respectively, and their respective sensitivity limits  $5.25 \times 10^{-18}$  and  $3.09 \times 10^{-18}$  erg s<sup>-1</sup>cm<sup>-2</sup>Å<sup>-1</sup> per pixel (see Bianchi et al. 2003 for further details on the NGC 2903 *GALEX* data).

Both the FUV and NUV images were aligned to the same coordinate system and pixel scale as the H $\alpha$  image and the background was subtracted in the same way as for the H $\alpha$  and *Spitzer* data.

### 2.2.4 Other data: ground-based optical images and CO ( $J=1-0$ )

Ground-based optical images from the *Sloan Digital Sky Survey* (SDSS) and a map of the CO ( $J=1-0$ ) rotational transition emission were also used for the morphological analysis of NGC 2903. The optical data set comprises  $g'$ ,  $r'$ , and  $z'$  band images, which were observed as part of the SDSS data release 6 and have a PSF FWHM of  $\sim 1.1''$ . We subtracted the sky emission from these images using the same IRAF script used for the H $\alpha$  image (Sec. 2.2.1).

For the photometric calibration, we estimated the calibration factor for converting the image digital counts to calibrated  $g'$ ,  $r'$ , and  $z'$  AB magnitudes as described on the SDSS web page for the data release 6<sup>2</sup>. These calibrated images were used to produce a  $g' - z'$  colour map of NGC 2903 (Fig. 2.2e).

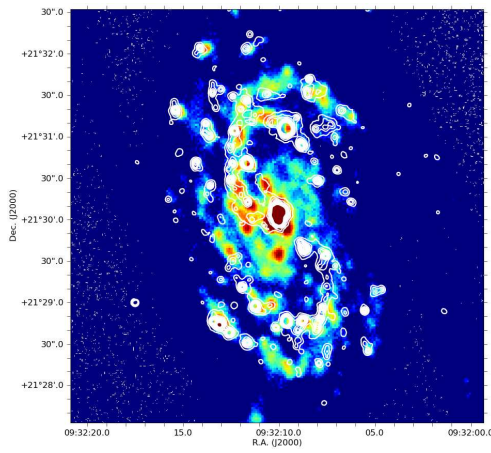
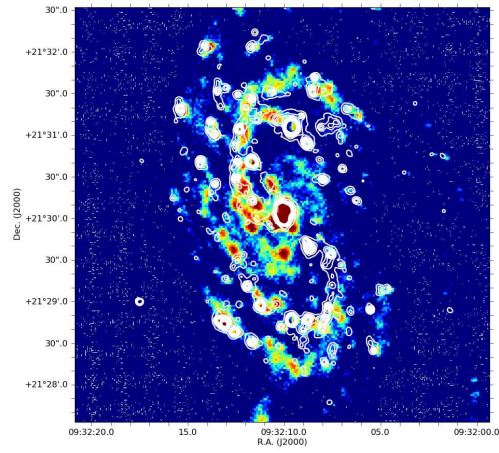
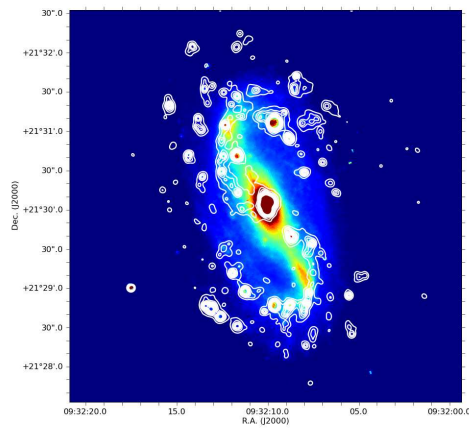
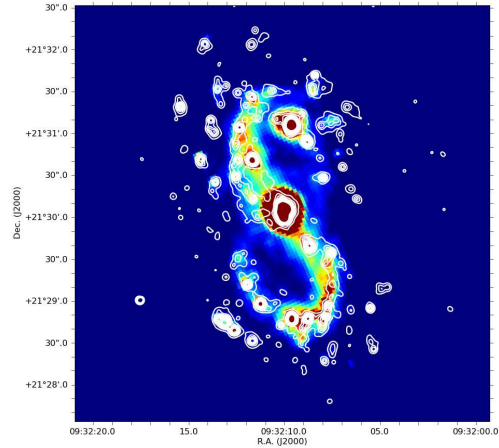
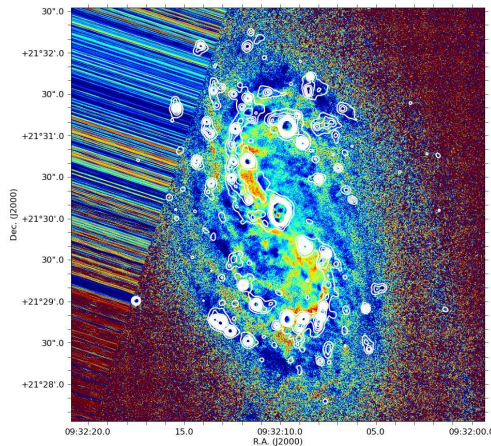
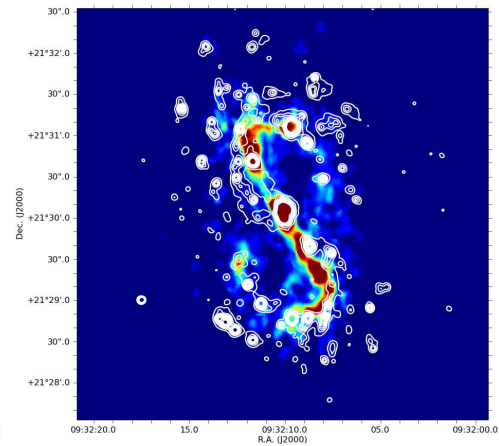
The CO ( $J=1-0$ ) emission-line map of NGC 2903 was used to trace the molecular gas emission. It was obtained from the BIMA (Berkeley-Illinois-Maryl and Association) array and the NRAO (National Radio Astronomy Observatory)<sup>3</sup> 12m single-dish telescope, as part of the BIMA SONG key project. The emission-line map has a maximum FWHM of 6.8''. Data acquisition and reduction details can be found in Regan et al. (2001) and Helfer et al (2003).

## 2.3 The general morphology of NGC 2903

The different appearance of galaxies in different wavelength ranges has already been illustrated by many authors. Galaxies in the UV bands seem to be patchier and of later type than the same galaxies observed at optical and near-infrared wavelengths. Stellar components such as bulges,

<sup>2</sup><http://www.sdss.org/dr6/algorithms/fluxcal.html>

<sup>3</sup>The National Radio Astronomy Observatory is a facility of the NSF operated under cooperative agreement by Associated Universities, Inc.

NUV with overlaid  $H\alpha$  contours.FUV with overlaid  $H\alpha$  contours. $3.6 \mu\text{m}$  with overlaid  $H\alpha$  contours. $24 \mu\text{m}$  with overlaid  $H\alpha$  contours. $g' - z'$  colour map with overlaid  $H\alpha$  contours.CO ( $J=1-0$ ) with overlaid  $H\alpha$  contours.

**Figure 2.2:** Images of NGC 2903 in different spectral bands: (a) GALEX NUV image, logarithmic scale. (b) GALEX FUV image, logarithmic scale. (c) Spitzer  $3.6\mu\text{m}$ . (d) Spitzer  $24\mu\text{m}$ . (e)  $g' - z'$  colour-map. (f) CO ( $J=1-0$ ) transition map of NGC 2903. All the colour scales are given in arbitrary units. All images (a) to (f) show superimposed  $H\alpha$  contours, the resolution of each image is given in the text, Sec. 2.2. The  $H\alpha$  contour levels range between  $4.5 \times 10^{35}$  erg/s/pix and  $4.5 \times 10^{36}$  erg/s/pix (the  $H\alpha$  image pixel size is  $0.33''/\text{pix}$ ).

bars, and old stellar disks tend to disappear when observed in the UV range (e.g., Kuchinski et al. 2000). NGC 2903 provides a good example of this behaviour. Figure 2.2 shows NGC 2903 observed in different wavelength regimes: FUV, NUV,  $3.6 \mu\text{m}$ ,  $24 \mu\text{m}$ ,  $g' - z'$  colour map and a CO ( $J=1-0$ ) rotational transition emission-line map. All images contain superimposed  $\text{H}\alpha$  contours.

The UV distribution is patchy and spiral-like and does not resemble the smooth bar-like distribution shown in the  $3.6 \mu\text{m}$  image. The CO ( $J=1-0$ ) traces the  $3.6 \mu\text{m}$  emission, while the  $\text{H}\alpha$  follows an s-shape distribution that is also followed by the main dust-lanes, as shown by the  $g' - z'$  colour image. Dust spurs emerge from the main dust lanes at many locations.

The  $\text{H}\alpha$  emission leads the CO ( $J=1-0$ ) emission, taking into account that NGC 2903 rotates counter-clockwise (Hernandez et al. 2005), assuming trailing spiral arms.

## 2.4 Photometry of star-forming regions

### 2.4.1 H II region catalogue

To study the properties of the recent star-forming sites in the NGC 2903 bar, we produced a catalogue of the H II regions located in the bar zone (except the nucleus). We consider the bar zone to be the area covering the whole *lense region* (Kormendy 1979) as observed in the  $3.6 \mu\text{m}$  image (see Fig. 2.2c). The selection criteria for identifying a feature in the  $\text{H}\alpha$  image as an H II region is that the feature must have an area in pixels equal to or larger than the image spatial resolution (i.e;  $\text{area} \approx 32$  pixels; with a pixel size of  $0.33''/\text{pix}$ ), all pixels having an intensity of at least three times the r.m.s. noise above the local background intensity level. This selection criteria implies a detectability limit of  $\sim 8.3 \times 10^{37} \text{ erg s}^{-1}$ .

A total of 67 H II regions were catalogued and their positions, sizes, and luminosities were measured. We performed aperture photometry using GAIA<sup>4</sup>. Most of the catalogued regions are located in the s-shape region and its neighbourhood, a region which is closely related to the stellar bar. A representation of the catalogued H II regions can be seen in Fig. 2.3.

The H II region catalogue comprises the position, size, shape, and  $\text{H}\alpha + [\text{N II}]$  luminosity of the regions, and is presented in Table 2.2. The table contains the H II region identification number in Col. 1; the equatorial coordinates (Cols. 2 and 3). Col. 4 shows the radius in arcseconds; Cols. 5 and 6 the eccentricity and position angle (measured northwest) of the integration aperture, and Col. 7 shows the decimal logarithm of the Galactic extinction-corrected  $\text{H}\alpha + [\text{N II}]$  luminosity (not corrected for internal dust extinction).

---

<sup>4</sup>GAIA is a derivative of the Skycat catalogue and image display tool, developed as part of the VLT project at ESO. Skycat and GAIA are free software under the terms of the GNU copyright.

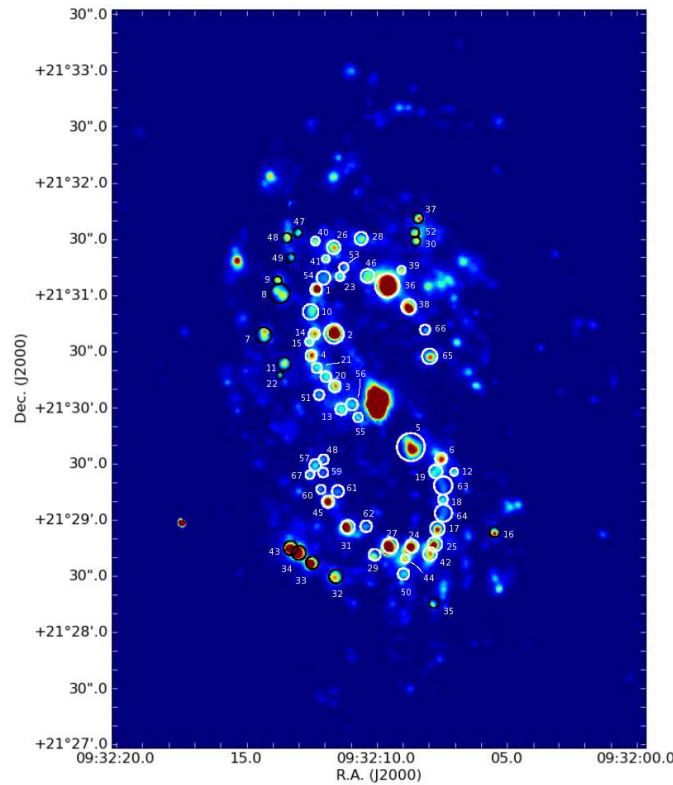


**Figure 2.3:**  $H\alpha$  continuum-subtracted image of NGC 2903. The white open circles indicate the position and size of the integration apertures of the catalogued  $H\text{II}$  regions belonging to the bar region. The black open circles indicate the  $H\text{II}$  regions closest to the catalogued UV complexes without  $H\alpha$  counterparts.

### $H\alpha$ equivalent width

The  $H\alpha$  equivalent width (hereinafter  $EW_{H\alpha}$ ) is a measure of the strength of the  $H\alpha$  emission with respect to the continuum emission of the stellar ionizing cluster. The  $EW_{H\alpha}$  depends not only mainly on the evolutionary stage of the  $H\text{II}$  region (decreasing as the region ages), but also on the metallicity, the IMF, dust content, and ionizing photon leakage (e.g., Bresolin & Kennicutt 1999; Zurita & Pérez 2008).

The  $H\alpha$  EWs were calculated from the ratio of our measured  $H\alpha$  luminosities (not corrected for internal dust extinction) to the continuum emission per  $\text{\AA}$ . The continuum emission of the ionizing cluster was estimated from the broad-band emission in the R-band at the position of the catalogued  $H\text{II}$  regions. Rather than using our Johnson R-band image of NGC 2903, we used the Sloan Digital Sky Survey (SDSS)  $r'$ -band image. The latter has a higher spatial resolution than our image, and therefore allowed us to more clearly identify and measure the continuum cluster emission.

When computing the  $H\alpha$  EW of an  $H\text{II}$  region, we are interested only in the continuum radiation emitted by the ionizing cluster. However, both the flux from the ionizing cluster and

the continuum emission from the underlying stellar population of the galaxy are included within the integration apertures. Correcting for this contamination is not straightforward and is the major source of uncertainty in H II region broad-band fluxes (Zurita & Pérez 2008). We followed the procedure described in Zurita & Pérez (2008) to estimate the contribution of the underlying stellar population to our measured broad-band fluxes by using two of the methods described there.

The first method consists of the measurement of the local background from the median value within annular apertures around the H II regions. The inner radius was set to be the effective radius of the H II region, and the annulus width to approximately three times the H II region radius.

The areas of the image corresponding to catalogued H II regions had previously been masked out in the image to avoid contamination within the annular apertures from neighbouring H II regions. For some regions, the median continuum emission within the annulus is clearly over-estimated causing an underestimation of the cluster continuum emission, which sometimes even results in negative fluxes. This is generally due to the strong spatial variations in the disk continuum emission on small scales. Therefore, a second approach was adopted to more tightly constrain the local background estimates.

The second method uses growth curves and takes advantage of the continuum emission in most H II regions being less extended than the H $\alpha$  emitting area. Therefore, the local background can be obtained from within the H II region area defined by its H $\alpha$  emission. For each H II region, we derived radially averaged  $r'$ -band surface-brightness profiles. For each region, we selected a radial range that was not contaminated by the ionizing cluster and determined the local background surface brightness from a fit to the profile in that range.

The  $r'$ -band continuum fluxes were all corrected for the underlying stellar population contamination using both methods (when possible), giving us two estimates of the  $r'$ -band flux of the ionizing cluster, from which we derived two values for the  $\text{EW}_{\text{H}\alpha+\text{[NII]}}$ . We calculated the difference between the two  $\text{EW}_{\text{H}\alpha+\text{[NII]}}$  estimates of each H II region, and this was taken to be the measured H $\alpha$ + [N II] EW uncertainty, so it represents the range of values covered when using the different estimates. Those regions for which the two estimates yielded differences larger than 600Å, and those regions for which only one background measurement was available, were discarded, as we considered the results non-reliable. The resulting H $\alpha$  EWs (including emission from the N II lines) are presented in Col. 8 of Table 2.2.

### 2.4.2 UV photometry

We performed aperture photometry on the NUV and FUV *GALEX* images to catalogue all the UV emitting knots of the bar region with the aim of obtaining their luminosities and colours. The aperture photometry was performed as described in Sec. 2.4.1 for the H II region catalogue, but using circular apertures centred on the FUV peaks. The location of the apertures is shown in

**Table 2.2:**  $H_{II}$  region catalogue of the bar zone of NGC 2903. Col. 1: ID number of the catalogued  $H_{II}$  regions; Cols. 2 and 3: equatorial coordinates; Col. 4:  $H_{II}$  region radius in arcseconds; Cols. 5 and 6: eccentricity and position angle (measured North-West) of the integration apertures; Col. 7: decimal logarithm of the  $H\alpha$  luminosity (in  $\text{erg s}^{-1}$ ); Col. 8: decimal logarithm of the  $H\alpha$  equivalent width; Col. 9: decimal logarithm of the  $24 \mu\text{m}$  emission within the  $H_{II}$  region apertures; Col. 10  $H\alpha$  attenuation see Sec. 2.4.3; Col. 11: estimate of the current star-formation rate for each catalogued  $H_{II}$  region. Cols. 7,8,9, and 10 include the corresponding correction for Galactic extinction (Schlegel et al. 1998). The SFRs were obtained after applying a correction of 25% for  $[N II]$  contamination to the  $H\alpha$  luminosities and dust extinction as given in Col. 10.

ID	R.A. (J2000)	Decl. (J2000)	Radius (arcsec)	$e$	P.A. (deg)	$\log L_{H\alpha+[NII]}$ (in $\text{erg s}^{-1}$ )	$\log EW_{H\alpha+[NII]}$ (in Å)	$\log(L_{24\mu\text{m}})$ (in $\text{erg s}^{-1}$ )	$A_{H\alpha}$ (mag)	SFR ( $10^{-3} M_{\odot} \text{yr}^{-1}$ )
1	09:32:12.35	21:31:04.66	3.1	0	90	38.99 ± 0.05	2.32 ± 0.11	40.60	1.21	17.7 ± 0.9
2	09:32:11.69	21:30:40.84	5.23	0.51	158	39.41 ± 0.05	2.86 ± 0.02	40.93	1.07	41.0 ± 2.2
3	09:32:11.67	21:30:12.75	3.17	0	0	38.71 ± 0.10	-	40.24	1.09	8.3 ± 0.9
4	09:32:12.56	21:30:29.23	3	0	0	38.75 ± 0.08	2.70 ± 0.09	40.19	0.95	7.9 ± 0.8
5	09:32:08.77	21:29:39.86	7.3	0.81	-28	39.28 ± 0.08	2.34 ± 0.04	40.71	0.93	26.5 ± 2.9
6	09:32:07.62	21:29:33.54	3.1	0	0	38.81 ± 0.08	3.07 ± 0.03	40.35	1.09	10.5 ± 0.9
7	09:32:14.38	21:30:40.38	4.23	0.68	6	38.76 ± 0.12	-	40.24	1.01	8.6 ± 1.2
8	09:32:13.75	21:31:02.56	5.23	0.8	-48	38.87 ± 0.11	-	39.49	0.21	5.3 ± 1.5
9	09:32:13.83	21:31:09.62	2.33	0	0	38.43 ± 0.10	2.50 ± 0.01	39.32	0.36	2.2 ± 0.5
10	09:32:12.57	21:30:52.67	4.17	0.77	10	38.60 ± 0.14	-	40.05	0.96	5.7 ± 1.0
11	09:32:13.60	21:30:24.86	3.7	0.52	38	38.62 ± 0.14	-	40.01	0.88	5.6 ± 1.1
12	09:32:07.12	21:29:26.37	2.03	0	0	38.12 ± 0.16	2.28 ± 0.01	39.65	1.08	2.1 ± 0.4
13	09:32:11.43	21:30:00.36	3.1	0	0	38.55 ± 0.14	-	39.97	0.92	4.9 ± 0.9
14	09:32:12.44	21:30:40.75	3	0	0	38.70 ± 0.09	2.43 ± 0.14	40.13	0.93	7.0 ± 0.8
15	09:32:12.63	21:30:36.70	2.23	0	0	38.30 ± 0.13	-	39.70	0.90	2.7 ± 0.5
16	09:32:05.59	21:28:54.01	2.8	0	90	38.59 ± 0.10	2.87 ± 0.03	39.77	0.61	4.1 ± 0.7
17	09:32:07.77	21:28:56.02	3.93	0	0	38.87 ± 0.11	-	40.51	1.27	14.1 ± 1.4
18	09:32:07.56	21:29:11.66	2.6	0	0	38.33 ± 0.16	-	40.23	1.74	6.4 ± 0.6
19	09:32:07.83	21:29:26.69	3.57	0	90	38.66 ± 0.14	-	40.32	1.30	9.0 ± 1.2
20	09:32:12.01	21:30:17.87	2.87	0.85	3	38.22 ± 0.13	-	39.79	1.14	2.8 ± 0.4
21	09:32:12.35	21:30:22.63	2.7	0.78	108	38.25 ± 0.13	2.60 ± 0.09	39.49	0.68	2.0 ± 0.4
22	09:32:13.76	21:30:18.72	1.9	0	0	38.00 ± 0.18	-	39.22	0.66	1.1 ± 0.3
23	09:32:11.44	21:31:11.46	2.33	0	90	38.30 ± 0.14	-	39.87	1.15	3.4 ± 0.5
24	09:32:08.76	21:28:46.76	3.53	0	90	39.10 ± 0.05	2.31 ± 0.04	40.50	0.89	16.8 ± 1.2
25	09:32:07.88	21:28:47.69	3.93	0	0	39.02 ± 0.07	2.63 ± 0.01	40.59	1.15	18.0 ± 1.4
26	09:32:11.67	21:31:27.14	3.6	0	0	38.77 ± 0.11	-	40.39	1.23	10.8 ± 1.2
27	09:32:09.59	21:28:47.12	4.17	0	0	39.41 ± 0.03	2.44 ± 0.02	40.93	1.08	40.8 ± 1.6
28	09:32:10.62	21:31:31.74	3.5	0	90	38.62 ± 0.15	2.56 ± 0.04	40.20	1.17	7.2 ± 1.1
29	09:32:10.18	21:28:42.26	3.1	0	90	38.52 ± 0.15	2.31 ± 0.03	40.13	1.21	6.0 ± 0.9
30	09:32:08.53	21:31:30.16	2.53	0	0	38.46 ± 0.11	2.44 ± 0.06	40.10	1.27	5.5 ± 0.6
31	09:32:11.20	21:28:57.28	3.67	0	0	39.19 ± 0.04	2.67 ± 0.03	40.59	0.89	20.7 ± 1.2
32	09:32:11.67	21:28:30.75	3.7	0	0	38.84 ± 0.10	2.67 ± 0.07	39.62	0.29	5.3 ± 1.3
33	09:32:12.57	21:28:38.22	3.5	0	0	39.14 ± 0.04	2.76 ± 0.02	40.56	0.91	19.1 ± 1.1
34	09:32:13.09	21:28:43.61	3.83	0	0	39.24 ± 0.04	2.49 ± 0.03	40.19	0.41	14.8 ± 1.4
35	09:32:07.93	21:28:16.18	2.67	0	0	38.34 ± 0.17	2.63 ± 0.00	39.73	0.88	2.9 ± 0.7
36	09:32:09.63	21:31:06.38	6.4	0	90	39.81 ± 0.03	2.51 ± 0.02	41.47	1.29	126.1 ± 3.8
37	09:32:08.43	21:31:42.49	2.8	0	90	38.61 ± 0.10	-	39.67	0.50	3.8 ± 0.7
38	09:32:08.81	21:30:55.01	4	0	0	39.14 ± 0.06	2.52 ± 0.08	40.51	0.85	17.8 ± 1.5
39	09:32:09.08	21:31:14.75	2.17	0	0	38.35 ± 0.11	-	40.07	1.41	4.9 ± 0.4
40	09:32:12.38	21:31:30.57	2.33	0	0	38.30 ± 0.14	-	38.98	0.24	1.5 ± 0.5
41	09:32:11.97	21:31:21.00	2	0	0	38.22 ± 0.12	-	39.68	0.98	2.4 ± 0.4
42	09:32:08.06	21:28:42.43	3.67	0	0	38.87 ± 0.09	2.25 ± 0.01	40.32	0.97	10.7 ± 1.2
43	09:32:13.40	21:28:46.21	3.83	0	0	39.16 ± 0.05	2.41 ± 0.03	40.20	0.48	13.4 ± 1.4
44	09:32:09.01	21:28:40.08	2.37	0	0	38.52 ± 0.09	-	40.38	1.67	9.2 ± 0.5
45	09:32:11.96	21:29:10.88	3.27	0	0	38.90 ± 0.07	2.64 ± 0.02	40.55	1.27	15.3 ± 1.0
46	09:32:10.39	21:31:11.67	3.7	0	0	38.79 ± 0.11	2.43 ± 0.04	40.42	1.25	11.5 ± 1.3
47	09:32:13.05	21:31:35.10	2.43	0	0	38.28 ± 0.16	2.85 ± 0.01	39.45	0.62	2.0 ± 0.5
48	09:32:13.47	21:31:32.35	2.7	0	0	38.53 ± 0.11	-	40.00	0.99	5.0 ± 0.7
49	09:32:13.32	21:31:21.74	2.4	0	0	38.19 ± 0.19	2.72 ± 0.09	39.47	0.73	1.8 ± 0.5
50	09:32:09.09	21:28:31.92	3.03	0	0	38.42 ± 0.18	-	40.34	1.80	8.1 ± 0.9
51	09:32:12.27	21:30:08.09	2.7	0.03	83	38.21 ± 0.23	-	39.72	1.04	2.5 ± 0.7
52	09:32:08.58	21:31:34.64	2.67	0	0	38.56 ± 0.10	-	40.10	1.09	5.9 ± 0.7
53	09:32:11.28	21:31:16.48	2.5	0	0	38.17 ± 0.21	2.21 ± 0.36	39.93	1.48	3.4 ± 0.6
54	09:32:12.06	21:31:11.01	3.67	0	0	38.53 ± 0.20	1.99 ± 0.11	40.29	1.47	7.8 ± 1.2
55	09:32:10.77	21:29:56.08	2.5	0	0	38.27 ± 0.17	1.85 ± 0.21	40.29	2.00	6.9 ± 0.6
56	09:32:11.01	21:30:03.02	3.2	0	0	38.51 ± 0.16	-	40.63	2.21	14.6 ± 0.9
57	09:32:12.42	21:29:30.64	3.17	0	0	38.47 ± 0.17	-	40.11	1.26	5.6 ± 0.9
58	09:32:12.10	21:29:33.70	2.67	0	0	38.18 ± 0.24	3.15 ± 0.07	39.70	1.06	2.4 ± 0.7
59	09:32:12.12	21:29:26.71	2.6	0	0	38.12 ± 0.26	-	39.78	1.30	2.6 ± 0.6
60	09:32:12.21	21:29:17.71	2.43	0	0	38.06 ± 0.26	-	39.92	1.67	3.2 ± 0.5
61	09:32:11.56	21:29:16.67	3.2	0	0	38.32 ± 0.25	2.85 ± 0.06	40.03	1.38	4.4 ± 0.9
62	09:32:10.49	21:28:57.76	3.07	0.55	61	38.27 ± 0.21	2.29 ± 0.05	39.43	0.60	1.9 ± 0.7
63	09:32:07.53	21:29:19.29	4.9	0.9	-18	38.33 ± 0.25	2.46 ± 0.04	40.10	1.50	5.0 ± 1.0
64	09:32:07.53	21:29:04.49	4.63	0.87	14	38.37 ± 0.23	-	40.16	1.54	5.8 ± 1.0
65	09:32:08.01	21:30:28.55	4.13	0	90	38.83 ± 0.13	-	39.96	0.56	6.7 ± 1.6
66	09:32:08.18	21:30:42.83	2.67	0	0	38.16 ± 0.25	-	39.09	0.39	1.2 ± 0.7
67	09:32:12.63	21:29:25.61	2.33	0	0	38.13 ± 0.21	-	39.50	0.86	1.7 ± 0.5

Fig. 2.4. The same apertures and centres were used to measure fluxes on the  $H\alpha$  and  $24\ \mu\text{m}$  with the aim of deriving the dust attenuation (Sec. 2.4.3). The aperture size selection, 13.2 arcsec, corresponding to  $\sim 570$  pc at the galaxy distance, was determined by the spatial resolution of the  $24\ \mu\text{m}$  image and the emission peak shifts of the emitting knots at the different bands (see below in this section). These large apertures can cause some overlap between integration areas of neighbouring regions, but in none of the cases is the contamination significant.

As already mentioned for the  $H\alpha$  photometry in Sec. 2.4.1, the background emission has to be subtracted from the measured  $24\ \mu\text{m}$ , NUV, and FUV fluxes within the aperture, to yield the stellar cluster emission alone. When estimating the background contamination, the annuli around each aperture are difficult to define because of crowding. As an alternative method, we fitted light profiles perpendicular to the bar major axis averaged over a rectangle of width  $\approx 40''$  (much larger than our photometric apertures for averaging out small-scale background variations, but small enough to ensure a valid local background estimate). The local background of each region was then obtained by interactive interpolation of the background on the corresponding fitted profile (second order polynomial) at the position of the emission peaks. A total of 56 regions were catalogued in the bar region alone (excluding the galaxy centre) and the positions, luminosities, and UV colours are shown in Table 2.3.

The peaks of emission in the UV and the  $24\ \mu\text{m}$  (and  $H\alpha$ ) image are offset from each other by a few arcseconds in most of the regions. This offset between the emission peaks in UV and  $24\ \mu\text{m}$  (and  $H\alpha$ ) amounts to  $6''$  and was already noticed by Calzetti et al. (2005) for M51.

As already said, the  $24\ \mu\text{m}$  and  $H\alpha$  emission peaks do not always fall within the UV apertures. Therefore, the  $H\alpha$  and  $24\ \mu\text{m}$  luminosities shown in Table 2.3 should be used with care, as they represent the luminosities of regions centered on the UV peaks with the unique aim of obtaining the dust attenuation in the UV. For the  $H\alpha$  luminosities of the  $H\text{II}$  regions, we refer the reader to Sec. 2.4.1 and Table 2.2. Last column of Table 2.3 shows the ID number of the  $H\text{II}$  region catalogue, which matches the UV emitting knot.

A careful visual inspection of the UV, the  $H\alpha$ , and the  $24\ \mu\text{m}$  images of NGC 2903 indicates that a number of compact bright UV emission knots, mainly located in the bar region, in the southeastern and northwestern area from the nucleus, have significant counterpart emission at neither  $H\alpha$  nor  $24\ \mu\text{m}$  wavelengths (see Fig. 2.2).

### 2.4.3 Dust attenuation

For many years, much effort has gone into deriving reliable and easy-to-use dust extinction indicators to correct optical and UV observations (e.g., Kennicutt 1983; Calzetti et al. 2000; Iglesias-Páramo et al. 2006). The appearance of multiwavelength observations from the FUV to the mid-infrared of a relatively large sample of nearby galaxies (e.g., SINGS; Kennicutt et al. 2003) allowed us to determine a reliable extinction correction using all the available bands. The  $H\alpha$  and  $24\ \mu\text{m}$  combination has been shown to be a very useful tool for estimating attenuation-

corrected  $H\alpha$  and UV fluxes (Kennicutt et al. 2007; Kennicutt et al. 2009). We used these results to obtain dust-corrected UV fluxes. We calculated the attenuation in the UV bands from the  $H\alpha$  attenuation using the laws presented by Calzetti (2001)

$$A_{0.16,star} = 1.78A_{H\alpha,gas} \quad (FUV)$$

$$A_{0.28,star} = 1.29A_{H\alpha,gas} \quad (NUV),$$

where  $A_X$  is the attenuation, in magnitudes, at the specific band. To obtain the  $H\alpha$  attenuation, we used the method described by Kennicutt et al. (2007)

$$A_{H\alpha} = 2.5 \log \left[ 1 + \frac{aL_{24\mu m}}{(L_{H\alpha})_{obs}} \right],$$

where  $(L_{H\alpha})_{obs}$  refers to the observed  $H\alpha$  luminosity with correction for the  $N\ II$  lines,  $L_{24\mu m}$  is defined as the product  $\nu L_\nu$ , and  $a$  is the  $L_{24\mu m}/L_{H\alpha}$  constant scaling factor, which is fitted empirically. A value of 0.038 was adopted for  $a$ , as derived in the same paper for the derivation

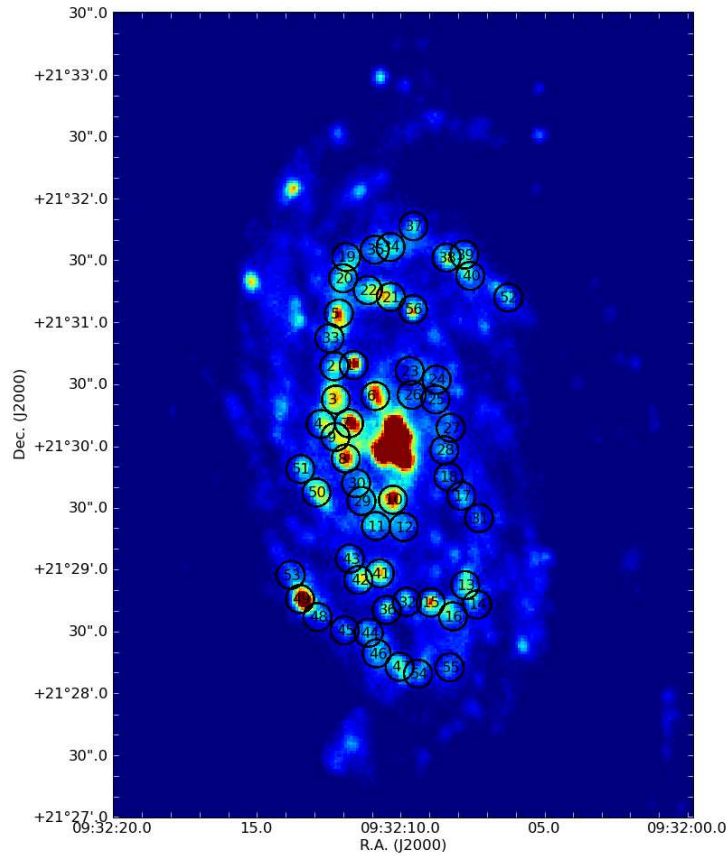


**Figure 2.4:** GALEX NUV image of NGC 2903 with the apertures used for photometry in the FUV, NUV,  $H\alpha$ , and  $24\ \mu m$  images. See Sec. 2.4.2 for further details.

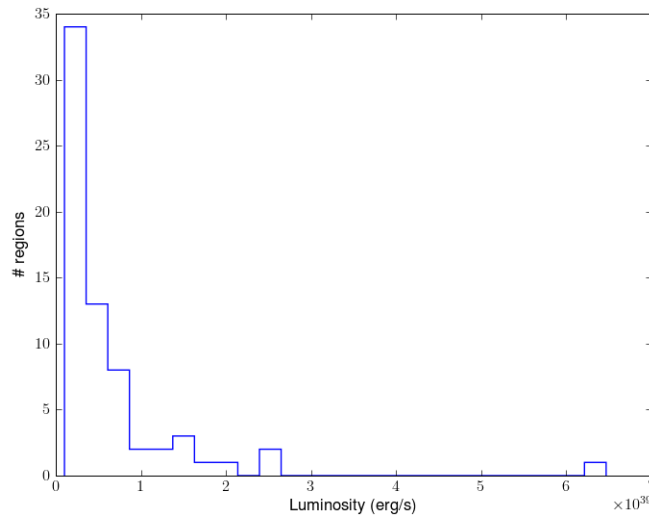


**Figure 2.5:** Distribution of the  $H\alpha + [N II]$  luminosity of the catalogued  $H II$  regions across the bar zone of NGC 2903 from which the  $EW_{H\alpha}$  were calculated.

of individual region parameters, and a value of  $a = 0.02$  was adopted when deriving galaxy integrated parameters. Galactic extinction was applied to the calculation of the dust attenuation. Errors in the attenuation and UV magnitudes follow from two uncertainties; first, the photometric calibration uncertainties and second, the local background estimates. Errors are of the order of 10%.

Because no dust tracers are detected in the UV emitting regions without  $H\alpha$  and  $24 \mu m$  emission counterparts, we adopted a value of zero for the attenuation in these regions. Besides the lack of  $H\alpha$  and  $24 \mu m$ , neither  $8 \mu m$  (Dale et al. 2009) nor CO ( $J=1-0$ ) emission is detected in these regions, indicating that there is very little gas or dust obscuring the UV emission. As an  $L_{H\alpha}$  upper limit for these regions we assumed  $L_{H\alpha+[NII]} = 3.8 \times 10^{38} \text{ erg s}^{-1}$ , which is the integrated  $H\alpha$  luminosity in a 13.2 arcsec aperture assuming a constant flux per pixel equal to the r.m.s. noise of the  $H\alpha$  image background. The derived  $H\alpha$  attenuations for the complete catalogue are presented in Table 2.3. We then derived UV-corrected magnitudes and calculated the FUV-NUV colour for each region. These results are also presented in Table 2.3: Col. 1 indicates the ID of the regions; Cols. 2 & 3 the equatorial coordinates; Cols. 4-7 the  $H\alpha$ ,  $24 \mu m$ , FUV, and NUV luminosities, respectively; Col. 8 the  $H\alpha$  attenuation; Cols. 9 and 10 the FUV and NUV attenuation-corrected magnitudes, respectively; Col. 11 the FUV - NUV colour derived; and Col. 12 the  $H II$  region ID (taken from table 2.2) located close to each of the corresponding UV knot.

**Table 2.3:** Summary of positions and photometry of the star-forming knots. Col. 1: ID of the regions; Cols. 2 & 3: right ascension and declination respectively; Cols. 4-7: decimal logarithm of the  $H\alpha$ ,  $24\ \mu\text{m}$  FUV and NUV luminosities respectively, these values have not been corrected for extinction; Col. 8: estimated  $H\alpha$  attenuation in magnitudes; Cols. 9 and 10: FUV and NUV attenuation-corrected magnitudes; Col. 11: the FUV-NUV colour of the star forming region. Col. 4 shows luminosities corrected for a 25%  $[N\ II]$  contamination. For the regions where Col. 8 has a value of 0.0, Cols. 4 and 5 correspond to an upper limit of the corresponding luminosities.

ID	R.A. (J2000)	Decl. (J2000)	$\log L_{H\alpha}$ ( $\text{erg s}^{-1}$ )	$\log L_{24\mu\text{m}}$ ( $\text{erg s}^{-1}$ )	$\log L_{FUV}$ ( $\text{erg s}^{-1}$ )	$\log L_{NUV}$ ( $\text{erg s}^{-1}$ )	$A_{H\alpha}$ (mag)	FUV (mag)	NUV (mag)	FUV - NUV (mag)	H $\alpha$ ID
1	09:32:11.67	21:30:40.80	39.15	40.92	40.63	40.73	1.27	15.74	15.67	0.08	2
2	09:32:12.34	21:30:40.00	38.93	40.57	40.53	40.61	1.06	16.37	16.22	0.15	14,15
3	09:32:12.25	21:30:23.80	38.87	40.32	40.80	40.83	0.78	16.19	16.03	0.16	4,20,21
4	09:32:12.75	21:30:11.70	<38.48	<39.41	40.65	40.58	0	17.95	17.68	0.27	-
5	09:32:12.23	21:31:05.70	38.94	40.71	40.74	40.81	1.29	15.44	15.45	-0.01	1
6	09:32:10.89	21:30:26.10	38.65	40.47	40.69	40.83	1.36	15.44	15.30	0.14	-
7	09:32:11.78	21:30:12.50	38.86	40.32	40.90	40.91	0.8	15.89	15.81	0.08	2,3
8	09:32:11.85	21:29:55.30	<38.48	<39.53	40.77	40.80	0	17.65	17.13	0.52	13
9	09:32:12.23	21:30:05.70	<38.48	<39.75	40.71	40.74	0	17.79	17.26	0.53	51
10	09:32:10.18	21:29:35.90	<38.48	<39.82	40.79	40.87	0	17.59	16.95	0.64	-
11	09:32:10.74	21:29:22.90	<38.48	<38.94	40.41	40.54	0	18.55	17.78	0.77	-
12	09:32:09.78	21:29:22.80	<38.48	<39.53	40.32	40.41	0	18.77	18.10	0.67	-
13	09:32:07.59	21:28:55.40	38.97	40.64	40.52	40.64	1.11	16.29	16.08	0.21	17
14	09:32:07.16	21:28:46.10	38.75	40.03	40.43	40.46	0.6	17.45	17.21	0.23	25
15	09:32:08.77	21:28:46.40	39.17	40.84	40.64	40.71	1.1	16.00	15.91	0.09	24
16	09:32:07.98	21:28:40.00	38.88	40.51	40.54	40.59	1.06	16.35	16.29	0.06	42
17	09:32:07.81	21:29:38.70	38.90	40.38	40.09	40.23	0.83	17.88	17.49	0.39	-
18	09:32:08.27	21:29:47.70	38.87	40.26	40.05	40.14	0.71	18.18	17.86	0.33	-
19	09:32:12.03	21:31:33.30	38.70	40.34	40.54	40.58	1.07	16.31	16.31	0.01	26
20	09:32:12.12	21:31:22.90	38.70	40.49	40.64	40.68	1.32	15.63	15.72	-0.1	41
21	09:32:10.45	21:31:14.50	38.83	40.70	40.65	40.75	1.45	15.36	15.38	-0.03	46
22	09:32:11.25	21:31:17.50	38.78	40.39	40.62	40.74	1.02	16.20	15.95	0.25	23
23	09:32:09.72	21:30:38.80	<38.48	<39.53	40.19	40.34	0	19.10	18.27	0.82	-
24	09:32:08.78	21:30:34.90	<38.48	<39.84	40.26	40.27	0	18.91	18.44	0.48	-
25	09:32:08.80	21:30:25.20	<38.48	<39.94	40.17	40.20	0	19.15	18.63	0.52	-
26	09:32:09.63	21:30:27.20	<38.48	<40.07	40.12	40.27	0	19.28	18.44	0.84	-
27	09:32:08.25	21:30:11.70	<38.48	<39.85	40.09	40.06	0	19.35	18.96	0.39	-
28	09:32:08.45	21:30:00.70	<38.48	<40.06	40.17	40.20	0	19.16	18.61	0.55	-
29	09:32:11.27	21:29:34.90	<38.48	<39.52	40.37	40.44	0	18.64	18.02	0.62	-
30	09:32:11.47	21:29:43.50	<38.48	<39.81	40.39	40.36	0	18.59	18.22	0.37	-
31	09:32:07.17	21:29:28.20	38.83	40.24	39.79	39.94	0.74	18.77	18.31	0.46	6
32	09:32:09.60	21:28:46.50	39.16	41.03	40.37	40.44	1.45	16.06	16.16	-0.09	27
33	09:32:12.54	21:30:53.60	38.76	40.63	40.45	40.59	1.46	15.84	15.75	0.09	10
34	09:32:10.51	21:31:38.80	<38.48	<40.07	40.58	40.64	0	18.12	17.54	0.59	28
35	09:32:11.05	21:31:37.20	<38.48	<40.19	40.54	40.58	0	18.22	17.67	0.56	-
36	09:32:10.29	21:28:42.20	38.62	40.53	40.40	40.47	1.53	15.84	15.98	-0.14	29
37	09:32:09.74	21:31:49.20	<38.48	<39.48	40.42	40.49	0	18.52	17.89	0.63	-
38	09:32:08.56	21:31:34.30	38.76	40.44	40.61	40.65	1.12	16.05	16.06	-0.01	30,52
39	09:32:07.94	21:31:36.10	38.82	40.01	40.59	40.61	0.5	17.20	16.97	0.23	37
40	09:32:07.72	21:31:25.80	<38.48	<39.31	40.54	40.60	0	18.22	17.63	0.59	-
41	09:32:10.56	21:28:59.90	38.92	40.38	40.67	40.72	0.81	16.48	16.28	0.19	-
42	09:32:11.30	21:28:56.40	38.90	40.76	40.64	40.66	1.42	15.46	15.64	-0.18	31
43	09:32:11.61	21:29:06.70	38.75	40.52	40.47	40.51	1.27	16.15	16.20	-0.05	45
44	09:32:10.89	21:28:30.90	<38.48	<40.03	40.52	40.52	0	18.28	17.82	0.47	-
45	09:32:11.72	21:28:31.70	38.74	40.16	40.39	40.36	0.76	17.26	17.24	0.01	32
46	09:32:10.59	21:28:21.00	<38.48	<39.53	40.55	40.57	0	18.20	17.71	0.49	-
47	09:32:09.78	21:28:14.80	<38.48	<39.74	40.64	40.60	0	17.97	17.61	0.36	-
48	09:32:12.68	21:28:37.90	39.01	40.57	40.54	40.53	0.94	16.55	16.59	-0.04	33
49	09:32:13.30	21:28:46.40	39.07	40.46	41.10	41.04	0.72	15.54	15.60	-0.06	34,43
50	09:32:12.83	21:29:38.40	38.48	39.71	40.66	40.59	0	17.92	17.64	0.28	-
51	09:32:13.41	21:29:49.60	<38.48	<39.63	40.40	40.33	0	18.57	18.29	0.28	-
52	09:32:06.38	21:31:15.80	38.65	39.77	40.42	40.44	0.43	17.75	17.47	0.28	-
53	09:32:13.65	21:28:58.00	<38.48	<39.77	40.47	40.49	0	18.39	17.90	0.49	-
54	09:32:09.14	21:28:11.60	<38.48	<39.98	40.48	40.47	0	18.38	17.95	0.43	-
55	09:32:08.05	21:28:15.20	<38.48	<40.14	40.30	40.40	0	18.82	18.11	0.71	35
56	09:32:09.67	21:31:08.80	39.42	41.32	40.25	40.44	1.5	16.26	16.08	0.18	36

## 2.5 Results

### 2.5.1 H $\alpha$ luminosity and EW $_{H\alpha}$

The logarithms of the H $\alpha$  +[NII] luminosities of the H II regions of NGC 2903 range from 38.0 to 39.8 erg s $^{-1}$  and their distribution is shown in a histogram in Fig. 2.5. The luminosities are within the range of typical values for extragalactic H II regions in barred and unbarred galaxies (see e.g., Kennicutt et al. 1989; Mayya 1994; González-Delgado & Pérez 1997; Rozas et al. 1999; Relaño et al. 2005), but are higher than the H $\alpha$  luminosities reported by Alonso-Herrero et al. (2001) for the nuclear region of NGC 2903. This apparent discrepancy is partly caused by the smaller distance assumed for NGC 2903 by these authors (6.3 Mpc versus 8.9 Mpc assumed in this paper). More importantly, Alonso-Herrero et al. (2001) apply a semi-automated method based on a limiting H $\alpha$  surface brightness to define the edges of an H II region from an *HST* image, yielding catalogued H $\alpha$  knots that may correspond to parts of a single H II region, as defined in ground-based H $\alpha$  imaging, and therefore have lower luminosities and sizes.

The H II region number 36, located in the northernmost part of the bar (see Table 2.2 and/or Fig. 2.3), has an H $\alpha$  luminosity of  $6.4 \times 10^{39}$  erg s $^{-1}$ , which makes this region the brightest H II region in the galaxy (outside the nuclear region of the galaxy). Its luminosity is comparable to, for instance the brightest H II region in the nearby spiral galaxy M51 (Calzetti et al. 2005; Scoville et al. 2001) and 30 Doradus in the Large Magellanic Cloud (Kennicutt et al. 1989).

The EW $_{H\alpha+[NII]}$  of H II regions in the bar of NGC 2903 range from  $\sim 71$  to  $\sim 1550$  Å, which is typical of disk and bar H II regions (e.g., Bresolin & Kennicutt 1999; von Hippel & Bothum 1990; Cedrés et al. 2005; Zurita & Pérez 2008). The distribution of EW $_{H\alpha+[NII]}$  has a mean value of  $\log \text{EW}_{H\alpha+[NII]} = 2.6 \pm 0.3$  (EW $_{H\alpha}$  in Å).

The H $\alpha$  equivalent width of H II regions depends on several factors including the initial mass function (IMF), the evolutionary status of the H II region, its metal content, and ionizing photon loss due to dust extinction or leakage from the region. Zurita & Pérez (2008) analysed the effect of all these factors on the observed distribution of EW $_{H\alpha}$  for the bar H II regions in NGC 1530, and we refer the reader to that paper for a more detailed discussion of the subject. Assuming similar physical conditions in the bar of NGC 2903, the evolutionary status of the H II region is the dominant factor affecting the EW $_{H\alpha}$  distribution. Assuming also that the H II region is the product of a single burst of star-formation, population synthesis models such as *Starburst99* (Leitherer et al. 1999) can be used to estimate an average age for each H II region, for a given IMF and metallicity. We therefore compared the theoretical predictions of *Starburst99* for the evolution of a single burst of star-formation with age, with our EW $_{H\alpha}$  measurements. Our *Starburst99* simulations used the Geneva stellar-evolutionary tracks, and a metallicity of  $Z = 0.02$  was assumed, which is the mean oxygen abundance of the gas in NGC 2903 at the range of galactocentric distances covered by the NGC 2903 bar (Pilyugin et al. 2004). For the IMF, we assumed a multi power-law parametrization ( $dN/dm \propto m^{-\alpha}$ ) with  $\alpha = 1.35$  for  $0.1 < M < 0.5M_{\odot}$  and  $\alpha = 2.35$

(Salpeter) for higher masses up to  $100M_{\odot}$ . From the comparison of the *Starburst99* output with our measurements (after correcting for [N II] contamination), we estimate that the ages of the catalogued H II regions of NGC 2903 are between 2.7 Myr ( $\log EW_{H\alpha} = 3.07$ ) and 7.1 Myr ( $\log EW_{H\alpha} = 1.73$ ). We note that to derive an age from the measured equivalent width, we first had to correct the measured equivalent width of the [N II] lines contribution.

Figure 2.6 shows the distribution of the  $EW_{H\alpha}$  in the galaxy on top of  $3.6 \mu\text{m}$  intensity contours. As mentioned earlier, the  $3.6 \mu\text{m}$  emission is a strong tracer of old underlying stellar populations and therefore a good indicator of the stellar bar. The distribution of the  $EW_{H\alpha}$  shows no correlation with position within the bar.

### 2.5.2 Dust attenuation

Figure 2.8 presents the distribution and amplitude of the  $H\alpha$  attenuation in the bar of NGC 2903 with the  $3.6 \mu\text{m}$  intensity contours (tracing the stellar bar) overlaid on top. The attenuation was calculated from the ratio of the  $H\alpha$  to the  $24 \mu\text{m}$  emission (Kennicutt et al. 2007) as presented in Sec. 2.4.3. The apertures are centered on regions of strong UV emission.

The mean attenuation value is around  $A_{H\alpha} \sim 1.0$  mag and ranges from 0 to 1.5 mag (except for regions 55 and 56, closer to the nucleus with an attenuation value of 2.2). There are a few UV regions where we assume no dust attenuation because of a lack of any significant  $H\alpha$  and  $24 \mu\text{m}$  emission (see Sec. 2.4.3). The higher attenuation values are located in the bar and at the beginning of the spiral pattern (see Table 2.3). This indicates that the bar and spiral arms in NGC 2903 are gas rich, whereas the UV emitting regions to the northwest and southeast of the galaxy nucleus, those regions with zero attenuation, have low gas and dust content; nevertheless, this region is populated by young stellar clusters, see Sec. 2.5.4. Additional discussion of the origin of these regions is presented in Sec. 2.6.

### 2.5.3 Star-formation rate

The locations of the most active star-formation sites within a bar are determined by the favoured dynamical behaviour of the gas and dust. Studying the distribution of the loci of current star-formation within bars can therefore put constraints on the properties of a particular bar potential. Gas does not stay in typical bar intersecting orbits and tends to accumulate and shock in certain regions of the bar. Dust lanes can be used as tracers of shocks in the gas flow (Athanasoula 1992). From Fig. 2.2, one can already see that the dust lanes (as seen from the  $g' - z'$  colour map) follow the CO (J=1-0) distribution, the  $H\alpha$  leading the CO (J=1-0) as previously observed in other barred spirals (e.g., Sheth et al. 2002). The  $H\alpha$  emission in the bar of NGC 2903 follows an s-shape covering the whole stellar bar and is dominated by classical localised H II regions (Fig. 2.3).

In ionization-bounded H II regions, the reddening-corrected  $H\alpha$  luminosity scales directly

with the total Lyman continuum flux emitted by the ionizing embedded star cluster. Therefore, the  $H\alpha$  emission is a good tracer of current star-formation. We used the following calibration relating the  $H\alpha$  luminosity to the rate of star-formation (Kennicutt 1998)

$$\text{SFR}_{H\alpha} (M_{\odot} \text{ year}^{-1}) = 7.9 \times 10^{-42} L_{H\alpha} (\text{erg s}^{-1}),$$

for calculating the current SFR associated with each catalogued H II region (Sec. 2.4.1). The results are given in Col. 11 of Table 2.2 and were obtained from the observed  $H\alpha$  luminosities (Col. 4 of Table 2.2), and were corrected for [N II] emission-lines contamination (see Sec. 2.2.1) and dust extinction inside the regions. The latter were estimated as already described in Sec. 2.4.3 for the UV emitting knots, comparing the  $H\alpha$  and  $24 \mu\text{m}$  luminosities within the H II region apertures. Given the different spatial resolution of the two images, we applied an aperture correction factor (Table 1 of Engelbracht et al. 2007). The SFRs obtained for our catalogued H II regions range from  $\sim 1.1$  to  $\sim 126 \times 10^{-3} M_{\odot} \text{ year}^{-1}$ . We excluded regions 55 and 56 in this calculation because of likely contamination from the nuclear region emission.

The total SFR implied by the  $H\alpha$  emission of the bar zone of NGC 2903 (excluding the nucleus) is  $\sim 0.9 \pm 0.2 M_{\odot} \text{ yr}^{-1}$  (Fig. 2.7 shows the integration area). This value implies that the NGC 2903 bar is forming stars at a rate comparable to other normal (non–starburst) spirals. The nucleus of NGC 2903 is almost as bright in  $H\alpha$  as the whole bar, implying that it hosts similar SFRs (Alonso–Herrero et al. 2001; Leon et al. 2008).

Alternative SFR calibrations make use of the UV emission. We derived the integrated SFR, within the same region as for the calculation of the  $\text{SFR}_{H\alpha}$ , using the UV emission as SF indicator. The SFR in the UV has been computed following the recipes given in Salim et al. (2007)

$$\text{SFR}_{UV} (M_{\odot} \text{ year}^{-1}) = 1.08 \times 10^{-28} L_{FUV},$$

with  $L_{FUV}$  in  $\text{ergs s}^{-1} \text{Hz}^{-1}$ . The star-formation rates calculated in this way infer a  $\text{SFR}_{FUV} = 0.44 \pm 0.06 M_{\odot} \text{ yr}^{-1}$  for the bar region. The SFR calculated from both bands (cf.  $\text{SFR}_{UV} = 0.44 \pm 0.06 M_{\odot} \text{ yr}^{-1}$  and  $\text{SFR}_{H\alpha} = 0.9 \pm 0.2 M_{\odot} \text{ yr}^{-1}$ ) and the fluxes from which these SFR were obtained, are compatible with the results given by other works based on a large number of galaxies (i.e; Lee et al 2009; Salim et al 2007). The  $\text{SFR}_{UV}$  is a tracer of *recent* star-formation, averaged over some hundreds of Myrs (Calzetti et al 2005; Kong et al. 2004), while the  $\text{SFR}_{H\alpha}$  probes the *current* star-formation. The SFRs derived in this paper are compatible with a number of star-formation histories, as derived from the *Starburst99* model. It is, however, interesting to date the age of the UV complexes with no  $H\alpha$  counterpart to shed some light into the origin of these structures. This is investigated in the next section.

## 2.5.4 UV colours and cluster ages

There is now a substantial amount of observational evidence that the  $FUV - NUV$  colours are very sensitive to the age of young stellar populations because of the rapid evolution of the most massive stars (i.e; Bianchi et al. 2006; Calzetti et al. 2005).

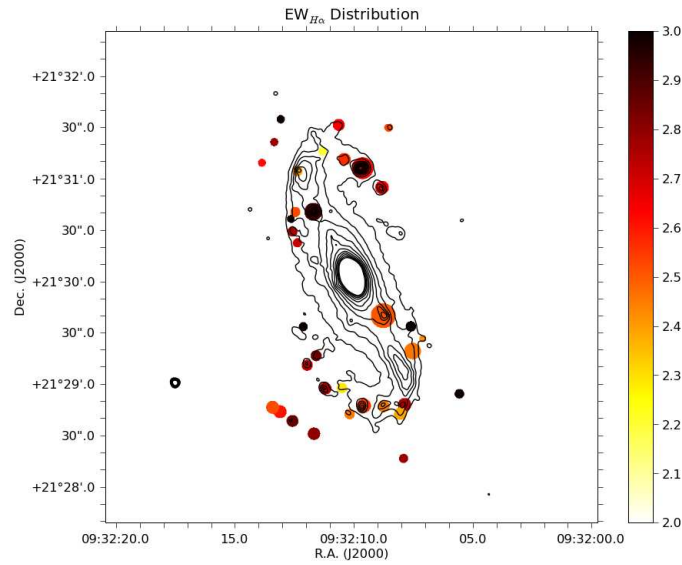


**Figure 2.6:**  $H\alpha + [N\text{II}]$  EW distribution in the bar region of NGC 2903. The size of the circles represents the  $H\text{II}$  region projected area. The intensity contours trace the  $3.6\ \mu\text{m}$  emission.

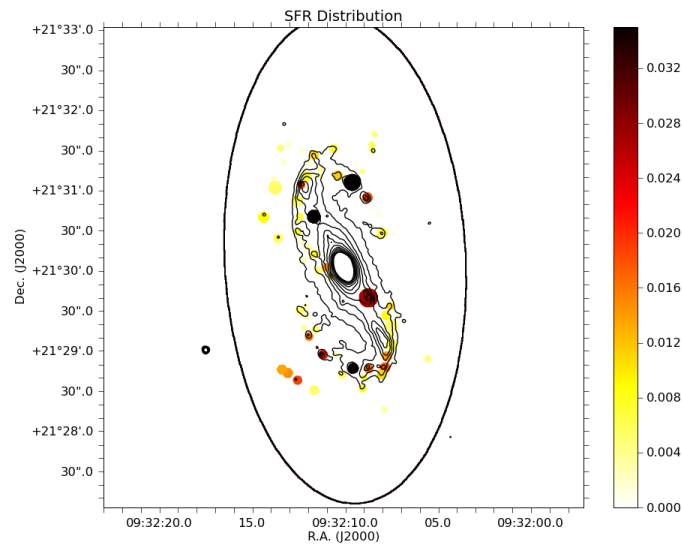


**Figure 2.7:** SFR distribution in the bar region of NGC 2903. The size of the circles represents the  $H\text{II}$  region projected area. The SFR is given in  $M_{\odot}\text{yr}^{-1}$ . The SFR was estimated from the measured  $H\alpha$  luminosity of the  $H\text{II}$  regions (see Sec. 2.5.3). The intensity contours trace the  $3.6\ \mu\text{m}$  emission. The solid black line indicates the integration area for the calculation of the total SFR in the bar region (see Sec. 2.5.3)

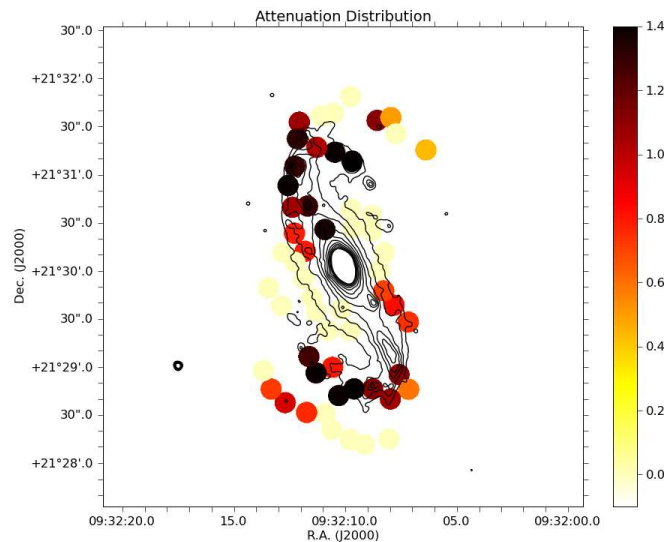


**Figure 2.8:** Distribution of the  $H\alpha$  attenuation in NGC 2903. The circle size represents the integration apertures used for the UV catalogue. The intensity contours trace the  $3.6\ \mu\text{m}$  emission.

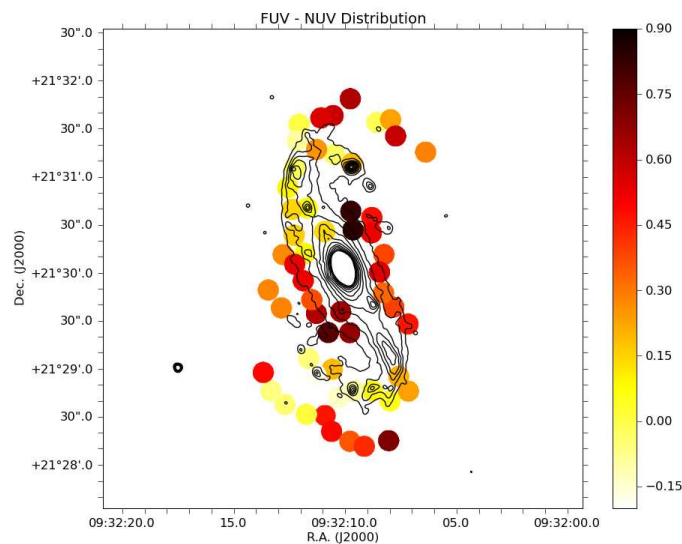


**Figure 2.9:** Distribution of the UV colours in the NGC 2903 bar and its surrounding regions. The intensity contours trace the  $3.6\ \mu\text{m}$  emission. A concentration of redder regions is clearly visible to the northeast and southwest of the nucleus. These regions correspond to the UV regions with no significant  $H\alpha$  counterpart.

To estimate the ages of our catalogued UV regions, we used the  $FUV - NUV$  colours, which had been calculated using fluxes corrected for dust attenuation (Sec. 2.4.3). Figure 2.10 shows the range of UV colours in the bar of NGC 2903. The colours have a mean value of 0.3 mag with a standard deviation of 0.27 mag. This range of values is typical of spiral galaxies (Thilker et al.

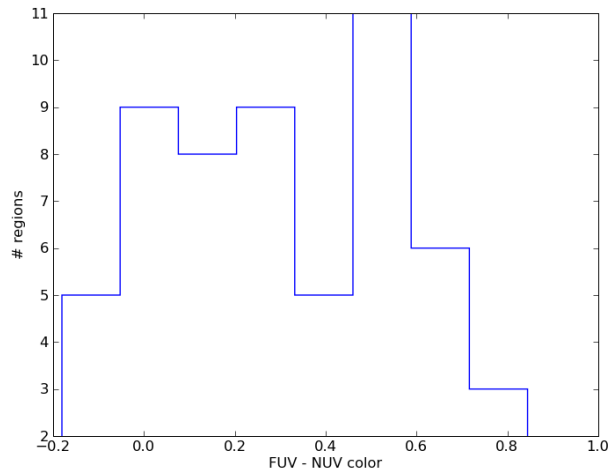


**Figure 2.10:** FUV - NUV colour distribution for the catalogued UV regions in the bar zone of NGC 2903.

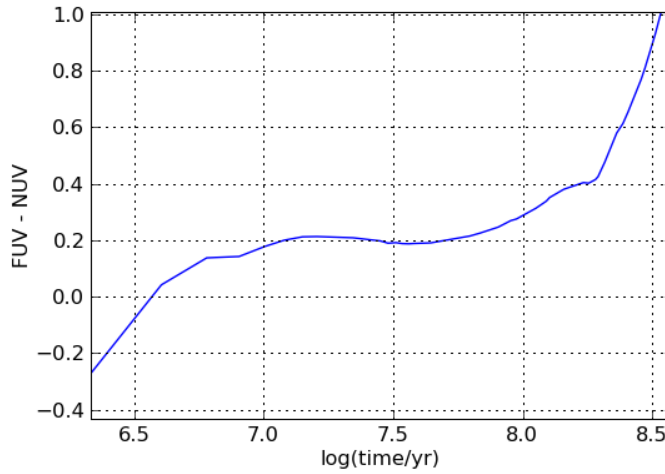


**Figure 2.11:** Time evolution of the UV colour for a single starburst region. The model assumes Padova stellar tracks with  $Z=0.02$  (solar) and an IMF constructed by a multi power-law parametrization with  $\alpha = 1.3$  for  $0.1 < M < 0.5M_{\odot}$  and  $\alpha = 2.35$  for higher masses up to  $100M_{\odot}$ .

2005; Koribalski & López-Sánchez 2009).

Figure 2.9 shows the spatial distribution of the derived *FUV* - *NUV* regions. One of the most striking properties of the colour distribution are the redder regions located to the northwest and southeast of the galaxy nucleus and at the beginning of the spiral arm. These regions correspond mostly to those with the lowest attenuation. The regions located along the bar consist mostly of blue UV emitting regions.

As well as being age-dependent, the *FUV* - *NUV* colours are also strong tracers of metallicity; however, we can assume an approximately constant metallicity in the bar region of NGC 2903

(Pilyugin et al. 2004). With this assumption, the  $FUV - NUV$  colour is, as we already mentioned, a good tracer of age. To compare our results with the theoretical models and then derive the ages of the clusters, we model the evolution of a single-star-formation burst using the *Starburst99* population synthesis model (Leitherer et al. 1999). As input values, we used the Padova AGB stellar tracks with a metallicity of  $Z = 0.02$  (solar). For the IMF, we assumed a multi power-law parametrization with  $\alpha = 1.3$  for  $0.1 < M < 0.5M_{\odot}$ , and  $\alpha = 2.35$  for higher masses up to  $100M_{\odot}$ . We then derived the  $FUV - NUV$  colours from the simulated spectrum in multiple time-steps of between 1 Myr and 1 Gyr (see Fig. 2.11).

To estimate the UV region ages, we interpolated the modelled  $FUV - NUV$  colour *versus* age dependence to the observed UV colours. The colours of the bluer regions range from -0.18 to 0.15, corresponding to an age of 3 to 10 Myr. The redder regions have colours ranging from 0.4 to 0.85, which imply ages ranging from  $\sim 150$  to 320 Myr. The latter group of colours corresponds to regions with significant amounts of neither  $H\alpha$  nor  $24 \mu\text{m}$  emission. The  $FUV - NUV$  colour remains constant around 0.2 implying ages of between 10 and a little younger than 100 Myr.

## 2.6 Discussion

NGC 2903 is a clear example of a galaxy with very different morphologies as shown by different broad-band images. Although its bar is classified in the NIR with a bar strength of 3 (Laurikainen & Salo 2002), corresponding to a relatively strong bar, and it is considered to be a *classical* bar, its morphology at shorter wavelengths is more similar to that of a patchy spiral disk. This clearly shows that to understand the SF history in bars it is necessary to obtain a panchromatic view.

To investigate the properties of SF in the NGC 2903 bar, we have at our disposal information about the distribution of gas in two different phases, namely the ionised gas and the colder CO ( $J = 1-0$ ). As for the stellar component, we are able to trace young stars up to 1 Gyr with the UV information, the location of massive stars can be traced from the location of their  $H II$  regions, whereas intermediate and older stellar populations can be probed according to their distribution in both the  $3.6 \mu\text{m}$  and optical bands.

We observe that the CO ( $J = 1-0$ ) distribution closely follows the emission in the  $3.6 \mu\text{m}$  band. There is a misalignment between the major axis of the bar derived from ellipse fitting of optical images (Sheth et al. 2002) and the  $3.6 \mu\text{m}$  major-axis light distribution. Both the CO ( $J = 1-0$ ) and the  $3.6 \mu\text{m}$  should therefore be on the leading side of the optical photometric axis of the bar. The  $H\alpha$  emission leads not only both the CO ( $J=1-0$ ) and the  $3.6 \mu\text{m}$  emission but has a slightly different distribution, following a spiral pattern not so clearly seen in the CO ( $J=1-0$ ) and  $3.6 \mu\text{m}$  emission. The  $H\alpha$  emission also leads the dust lanes as traced by optical colour maps. Numerical models predict that the gaseous component (of both ionised and neutral gas) leads the stellar bar (Martin & Friedli 1997).

This study started as a follow-up of the analysis carried out on the bar of NGC 1530 (Zurita

& Pérez 2008) to understand the physical processes determining star-formation in bars, where the importance of bar dynamics was clearly demonstrated. Both CO (J=1-0) and dust are concentrated in regions where shocks and gas accumulation are induced by the bar potential. The distribution of the dust in the bar of NGC 1530 is much narrower than the distribution in NGC 2903. In NGC 1530, the dust lanes are straight and clearly delineated as opposed to the broken feathery morphology of the dust lanes in NGC 2903 (Fig. 2.2e). This may indicate that no strong shocks are present in the bar of NGC 2903, in contrast to the large velocity gradients perpendicular to the bar in NGC 1530 (Zurita et al. 2004), suggesting that shocks are driving the observed morphology in NGC 1530.

Streaming motions along the bar of NGC 2903 were detected by Leon et al. (2008) using HCN(1-0) as the kinematic tracer. An ongoing analysis of the velocity gradients in the ionised gas of NGC 2903, using the data published by Hernandez et al. (2005), will clarify whether strong velocity gradients are present or not in the bar of NGC 2903. Therefore, although the NIR emission suggest that NGC 2903 hosts a strong bar, the broken and wide structure of the dust lanes may well be evidence that it does not.

The presence of H II regions in both the trailing and leading sides of the dust lanes in NGC 1530 and an age gradient between both sets of H II regions, provides support to the hypothesis (Sheth et al. 2002) that massive stars form in the trailing side of the bar dust lane and move to the leading side. There are no H II regions on the trailing side of the bar of NGC 2903, and no trend in H II region age is found across the bar. This may indicate that the explanation of where star-formation is favoured, is not as straightforward as in NGC 1530, or at least is not as clearly driven by the strong bar dynamics.

The complexity of the SF properties in the bar of NGC 2903 is also illustrated by the presence of compact UV sources without significant  $24\ \mu\text{m}$  and H $\alpha$  emission. These regions are located symmetrically with respect to the centre of the galaxy and nearly perpendicular to the bar as well as in a spiral pattern. All of these regions have *FUV* - *NUV* colours compatible with ages of a couple of hundred Myr. The lack of H $\alpha$  emission suggests that these locations are currently not favoured by the bar potential to form stars. These stars might have formed somewhere else in the bar and migrated afterwards to the current position. But then a few questions would arise: (1) where did these stars form?; (2) are the stars that are currently forming likely to remain at similar locations?; or, (3) in contrast, were they formed during a more general SF burst possibly linked to the bar formation, or a merger? An ongoing analysis of both the H I and H $\alpha$  velocity fields will shed some light onto the origin of the UV complexes.

The *current* SFR in the bar, as calculated from H $\alpha$ , is similar to those of other disk galaxies, although the bar contains a considerably high amount of dense cold gas, as traced by the HCN(1-0) (Leon et al. 2008). The *recent* SFR, as calculated from UV emission, is compatible with that of the *current* SFR.

We draw attention to the offsets of a few arcseconds between the emission peaks in the  $24\ \mu\text{m}$  and the *GALEX* images. The  $24\ \mu\text{m}$  emission is a good tracer of current star-formation, while

UV emission is a ‘time-averaged’ recent star-formation indicator (e.g., Calzetti et al 2005). The offsets found here (also seen in M51 by Calzetti et al 2005) indicate an evolutionary link between the sites where current star-formation is occurring and the position of the UV counterpart. Estimations of the rotation curve and the pattern speed would be necessary to determine whether the dynamical timescales are compatible with the ageing of the regions.

## 2.7 Summary and conclusions

We have performed a detailed multiwavelength study of observations from UV to sub–millimeter wavelengths of the NGC 2903 bar and its surrounding regions. We have mapped and catalogued the H II regions of the bar and measured their H $\alpha$  equivalent widths. Furthermore, we have obtained a catalogue of the UV emitting regions, and measured their peak locations with respect to those in the H $\alpha$  image. The extinction has been estimated using the H $\alpha$  and 24  $\mu$ m emission. Values of SFRs using both H $\alpha$  and UV indicators have been calculated. We have estimated the age of the regions, using the  $EW_{H\alpha}$  and the  $FUV - NUV$  colour together with stellar population synthesis models. Our main results are:

- NGC 2903 is a morphologically complex galaxy. Both the near–infrared and the CO ( $J=1-0$ ) band images detect a clear barred structure, whereas the H $\alpha$  and UV maps show a patchy spiral-like structure.
- There are clear spiral-like UV complexes with no significant H $\alpha$ , 24  $\mu$ m, and CO ( $J=1-0$ ) counterpart emission. These complexes are located northwest and Southeast of the bar within the inner 1 arcminute radius (corresponding to  $\sim 2.5$  kpc).
- The H $\alpha$  emission along the bar, leads the CO. The 3.6  $\mu$ m and CO ( $J=1-0$ ) emission trace each other, both leading the major axis of the optical light distribution.
- The H $\alpha$  luminosities and  $EW_{H\alpha}$  of the bar H II regions are within typical ranges for H II regions in both bar and unbarred spirals. The spatial distribution of the H $\alpha$  EWs does not correlate with any morphological feature in the bar.
- The average dust attenuation in the bar area of NGC 2903 is  $A_{H\alpha} = 1.06$ , and ranges from 0 to 1.5 mag.
- The  $FUV - NUV$  colour distribution is distributed into two regions. The bluer regions range from -0.18 to 0.15 implying an age of between  $\sim 3$  and 10 Myr. The redder regions have colours ranging from 0.4 to 0.85, which imply ages ranging from 150 to 400 Myr. The latter correspond to regions with significant amounts of neither H $\alpha$  nor 24  $\mu$ m emission.

- The SFRs of the bar region derived from both H $\alpha$  and the UV emission are  $0.9 \pm 0.2 M_{\odot} \text{yr}^{-1}$  and  $0.4 \pm 0.1 M_{\odot} \text{yr}^{-1}$ , respectively.

All these results suggest that some process triggered a SF burst a few hundred Myrs ago. Interestingly, we do detect some stellar clusters unrelated to the current SF locations, symmetrically located nearly perpendicular to the bar (in the inner  $\sim 2.5$  kpc). These regions might originate from this SF burst.

In a future paper, we will analyse the gas kinematics of the galaxy, with the aim of shedding some light on the origin (merger versus secular evolution) of these findings.

## Acknowledgements

G. Popping acknowledges support by the Stichting Groninger Universiteitsfonds. I. Pérez acknowledges support by the Netherlands Organisation for Scientific Research (NWO, Veni-Grant 639.041.511). I. Pérez & A. Zurita acknowledge support from the Spanish Plan Nacional del Espacio de Ministerio de Educación y Ciencia (via grant C-CONSOLIDER AYA 2007-67625-C02-02). I. Pérez & A. Zurita also thank the Junta de Andalucía for support through the FQM-108 project. We would like to thank Jorge Iglesias, Mónica Relaño, Ute Lisenfeld and Hervé Wozniak for the fruitful discussions. We thank the referee for the very useful comments and suggestions that have greatly improved the manuscript.



---

# Links between star-formation and H<sub>I</sub> and H $\alpha$ gas kinematics in NGC 2903

– G. Popping, I. Pérez, J.M. van der Hulst & A. Zurita –

## Abstract

*In a previous work we found NGC 2903 to have a morphologically very complex appearance in different wavelength bands. There are several UV complexes in the bar of the galaxy with no counterpart H $\alpha$  and 24  $\mu$ m wavelength emission. These complexes have ages much older than the other UV complexes in the bar, and are regions currently not favoured by the bar potential to form stars. The spatial distribution of the age of star-forming sites does not correlate with any morphological feature of the bar.*

*We aim to understand the interplay between bar dynamics and star-formation in the bar of NGC 2903 and how this relates to other strong bars. Secondly, we seek for signatures in the H<sub>I</sub> and H $\alpha$  velocity fields of NGC 2903 that might be related with the complex morphological appearance of NGC 2903 in different wavelength bands and the UV complexes currently not favoured by the bar potential to form stars.*

*We use H<sub>I</sub> and H $\alpha$  interferometric data to measure the kinematics of the neutral and ionised gas in NGC 2903. We use the H<sub>I</sub> to characterise the overall kinematics and the H $\alpha$  to measure the non-circular motions present in the bar region.*

*We find NGC 2903 to have a velocity field typical for a disk galaxy with some signs of gas response to a bar potential. No strong velocity gradients and shocks are present in the bar region of the galaxy. On a global scale peaks in H $\alpha$  non-circular velocity and intensity (i.e., star-formation sites) overlay, and no sign of strong interaction due to the bar potential between the two is found. These results point out that the bar does not show the typical features associated to strong bars and indicate that the gas dynamics and star-formation are not strongly driven by the bar potential. Combined with previous work that doubts the bar strength, it suggests that the bar of NGC 2903 is much weaker than was measured from broad-band imaging. The H<sub>I</sub> distribution and velocity field contain several signs of a merger event. The neutral gas distribution is warped, lopsided, the rotation curve of the receding and approaching side of the galaxy are asymmetric, and a clear phase shift is present in the change of position angle of the receding and approaching side with radius. A merger event*

*might be the origin of the complex dynamical appearance of NGC 2903 and the bar strength that appears to be weaker than suggested from broad-band imaging.*

### 3.1 Introduction

Barred spirals can be used as a useful tool to investigate how material is driven towards the centre of a galaxy and how the flow of material favours or inhibits star-formation. Especially their extreme physical conditions make barred spirals perfect objects to study the relation between dynamics and star-formation.

The bar potential drives gas into non-circular intersecting orbits, resulting in regions of strong shocks and shear. During the last decade much effort has been put into linking the dynamics of bars and resulting kinematics of the gas to star-formation. A study of the interplay between the non-circular motions and star-formation can shed some light on general conditions favouring star-formation.

This interplay was extensively studied for the case of NGC 1530 by Reynaud & Downes (1998) using the CO transition-line and Zurita et al. (2004) using H $\alpha$  emission. The former found that strong velocity changes are anti-correlated with star-formation. The latter found that velocity changes due to shear inhibit star-formation, whereas velocity changes due to shocks enhance it. Their second main result was an anti-correlation between H $\alpha$  surface brightness and the highest non-circular motions in the bar. Zurita & Pérez (2008) found that the dust spurs at the trailing side of the major bar dust lane in NGC 1530 correlate spatially with strong velocity gradients, with strong gradients probably tracing gas flows. The bar H II region photometric and dynamic properties are compatible with a migration scenario from the trailing to the leading side of the bar after their formation.(Zurita & Pérez 2008). The NGC 1530 results support the hypothesis that stars form in dust spurs at the trailing side of the bar dust lane and move towards the leading side as they age (Sheth et al. 2000, 2002).

In a previous paper, we showed that this hypothesis does not necessarily hold for all barred spirals (Popping et al. 2010). In a thorough multiwavelength study from the UV to the infrared we observed that star-formation in NGC 2903 is presently located at the leading side of the major bar dust lane and we found no trend in the age of H II regions with respect to their location. On top of that, we found several strongly emitting UV knots located perpendicularly to the bar in a spiral like shape with a significant amount of neither H $\alpha$  nor 24  $\mu$ m wavelength emission. The complexes have ages much older than the other UV complexes in the bar, and are regions currently not favoured by the bar potential to form stars. These results demonstrated the need to understand the bar dynamics if one wants to understand star-formation in bars properly. This need was strengthened by the appearance of different morphologies of NGC 2903 as observed in different wavelength bands.

A close inspection of the kinematic behaviour of the gas in NGC 2903 might shed light on

how the star-formation locii and the complex morphology of the galaxy are determined by the bar dynamics. This allows us to address what causes the discrepancy with the hypothesis on star-formation locii and evolution in bars as proposed by Sheth et al. (2000, 2002).

The aim of this paper is twofold. Firstly, we will study the kinematics of ionised gas and trace the interplay between shocks, shear, dust spurs, and star-formation. It will allow us to determine whether the relation between gas kinematic behaviour and star-formation as observed for strongly barred spiral NGC 1530, also holds for the morphologically more complex NGC 2903. This is carried out by studying the non-circular motions of the ionised gas around H II regions. We use H I 21 cm line-emission to create a model for the NGC 2903 rotational velocity field and subtract the model from Fabry-Pérot H $\alpha$  imaging of the velocity field to obtain the non-circular motions of the ionised gas.

Secondly, we will seek for signatures in both the H I and H $\alpha$  velocity field of NGC 2903 that might have to do with the strong UV emitting knots not linked to the bar dynamics and complex morphology of NGC 2903 as observed in different wavelength bands.

NGC 2903 is a close by (8.9 Mpc; Drozdovsky & Karachentsev 2000) SBd galaxy. It is isolated from large companions and shows no signs of a major merger event (Irwin et al. 2009). The galaxy possesses a symmetric strong bar considered typical for this type of galaxies (Laurikainen & Salo 2002), although the broken and wide dust lane, combined with the spiral like morphology of the galaxy in the UV, might be evidence of a less strong bar (Popping et al. 2010). The bar contains a large amount of H II regions as traced by their H $\alpha$  emission along the whole bar (Sheth et al. 2002), which makes NGC 2903 a perfect object to study the link between ionised gas kinematics and star-formation. A CO(1-0) emission velocity map is available for this object (Helfer et al. 2003) and can, together with HCN(1-0) emission based velocity data (Léon et al. 2008), be used as a reference.

The outline of this paper is as follows. In Sec. 2 we present the data. In Sec. 3 we present the methodology to analyse the H I and present the H I rotation curve and non-circular velocity field. Sec. 4 describes the methodology to analyse the H $\alpha$  and contains the main results regarding the non-circular velocity and velocity gradients of the ionised gas. In Sec. 5 we discuss our results and we end with a summary and conclusions.

## 3.2 Data

### 3.2.1 H I data cube

In order to study the kinematics of NGC 2903 we used H I data from the WHISP survey<sup>1</sup> (Kamphuis et al. 1996; van der Hulst et al. 2001). A description of the data reduction and details of the

---

<sup>1</sup>The Westerbork H I Survey of Spiral and Irregular galaxies. Observations were carried out with the Westerbork Synthesis Radio Telescope by the Netherlands Foundation for Research in Astronomy

data cubes available are presented at [www.astro.rug.nl/~whisp](http://www.astro.rug.nl/~whisp). We used the 30 arcsec resolution data cube which has a r.m.s noise of 2.1 mJy/beam. The observations cover a velocity range of  $\sim 500 \text{ km s}^{-1}$  from 315.54 to 834.91  $\text{km s}^{-1}$  in 127 steps of 4.14  $\text{km s}^{-1}$ . The beam size of the telescope during observations was 23.4 arcsec.

In order to isolate the signal, we first created a smoothed data cube at 60 arcsec resolution using the SMOOTH task in the GIPSY package<sup>2</sup> from the initial data cube, such that the pixel scale was retained. Pixels in each channel of the 60 arcsec cube with a pixel-value less than three times the r.m.s. noise were marked as “low-signal”. Pixel-values in each channel of the 30 arcsec resolution cube were set to blank if the same pixel in the 60 arcsec cube was marked as “low-signal”. This resulted in a conditionally transferred data cube, created using the CONDIT task. We used PYBLOT to blank all areas which passed the previous step, but after inspection were considered noise.

We created a total intensity, velocity and velocity dispersion map of NGC 2903 from the 30 arcsec resolution cube using the XGAUFIT task in GIPSY. For each pixel we fitted a Gaussian-Hermite through the channel map with 2.5 times the r.m.s noise as a lower cutoff. The obtained intensity and velocity maps are presented in Figure 3.1.

### 3.2.2 $H\alpha$ data cube

We used  $H\alpha$  Fabry-Pérot observations of NGC 2903 from the BH $\alpha$ BAR<sup>3</sup> sample to achieve understanding on the motions of the ionised gas in the bar. Observations were obtained using the FaNTomM<sup>4</sup> instrument at the Observatoire du mont Mégantic with a pixel size of 1.6 arcsec. The observations cover a velocity range of  $\sim 325 \text{ km s}^{-1}$  from 388.92 to 715.3  $\text{km s}^{-1}$  in 48 steps of 6.96  $\text{km s}^{-1}$ . Each channel has a signal to noise ratio around  $S/N \approx 3$ .

A Fabry-Pérot interferometer will detect imaginary emission which is the result of an optical bias (free spectral range jump). Before isolating the signal from the noise, we manually blanked all the ‘non-real’ emission due to the free spectral range jump in each channel using PYBLOT.

Because of the “large” pixel size, the amount of pixels with significant data was not large. We therefore used a datacube smoothed to a resolution of 3 arcsec, which enlarged the emission area, without creating false emission and losing too much information on the morphology of the intensity and velocity field.

Separation of signal from noise in the datacube at 3 arcsec resolution was done in the same way as described in section 3.2.1. A smoothed data cube with a resolution of 10 arcsec was used for the CONDIT task. Instead of using the XGAUFIT task to create a velocity map, we used the MOMENTS task to obtain zeroth, first and second order  $H\alpha$  moment maps of NGC 2903. Moments maps were created, using only signal above three times the r.m.s. noise in five

<sup>2</sup>Groningen Image Processing System (van der Hulst et al. 1992; Vogelaar & Terlouw 2001)

<sup>3</sup>Big H $\alpha$  kinematical sample of BARred spiral galaxies (Hernandez et al. 2005)

<sup>4</sup>Fabry-Pérot of New Technology of the Observatoire du mont Mégantic ([www.astro.umontreal.ca/fantomm](http://www.astro.umontreal.ca/fantomm))

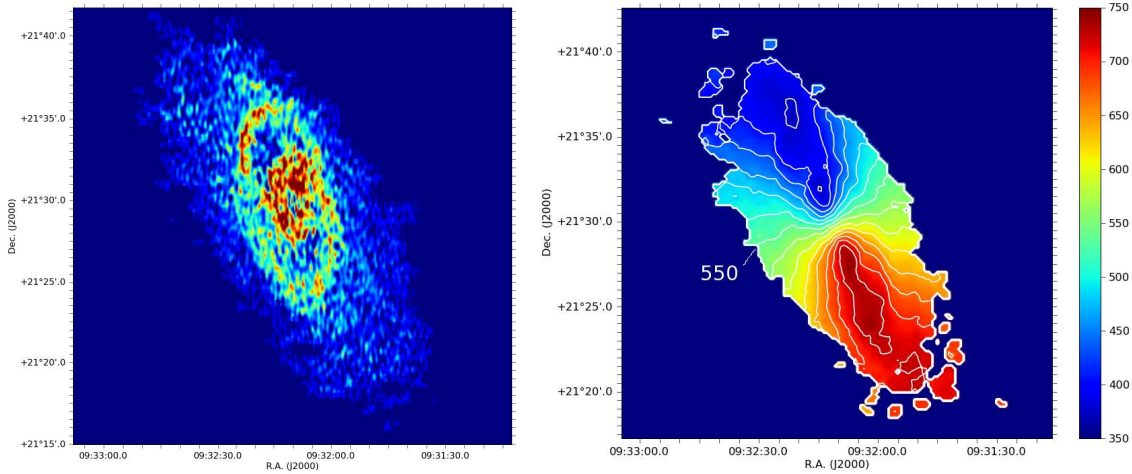


**Figure 3.1:** a)  $H\text{I}$  integrated intensity map of NGC 2903; b)  $H\text{I}$  velocity field of NGC 2903 in  $\text{km/s}$ . The contours range from  $350$  to  $750 \text{ km s}^{-1}$  with a step size of  $25 \text{ km s}^{-1}$ , the  $550 \text{ km s}^{-1}$  contour has been marked for clarity.

consecutive channels of the 3 arcsec data cube. We were not able to use the XGAUFIT task, since the  $H\alpha$  emission line profiles were noisy and not well described with a single Gaussian.

### 3.3 HI map and kinematics

The aim of usage of the  $H\text{I}$  map of NGC 2903 was twofold. Firstly, the  $H\text{I}$  cube was used to study the behaviour of neutral gas in NGC 2903. Secondly, we used the rotation curve to produce a two dimensional projection model of the velocity field in order to retrieve the  $H\text{I}$  and  $H\alpha$  non-circular motions. In this section we will focus on the  $H\text{I}$  general and kinematic properties of NGC 2903

#### 3.3.1 General $H\text{I}$ features

We find that most of the  $H\text{I}$  is concentrated in the inner disk (at a radius of  $\sim 200$  arcsec) and in a ring-like structure around this disk (see Figure 3.1a). The inner disk has a depletion of neutral gas in the galaxy centre. The ring-like structure coincides with the thin optical spiral arms in the outer parts of the galaxy (Begeman 1987). The galaxy has also a large  $H\text{I}$  envelope with an  $H\text{I}$  extent up to 3.2 times its optical diameter (Irwin et al. 2009). Lopsidedness is seen from the distribution of the neutral gas, as the Southern envelope goes out to a much larger extend than the Northern envelope. The large  $H\text{I}$  envelope is warped at both sides of the galaxy with respect to the ring-like structure and the inner disk. The increase in position angle with radius is prominent

in both sides of the galaxy.

The global profile of NGC 2903 is presented in Figure 3.2 and is in good agreement with previously published profiles (Irwin et al. 2009; Wong et al. 2006; Springob et al. 2005). We find a total H I mass of  $(48.00 \pm 0.04) \times 10^8 M_{\odot}$ . This mass is similar to the amount of neutral gas found by Irwin et al. (2009). Their H I map goes down to much lower sensitivity and to much larger extent, which implies that the outer H I envelope does not contribute significantly to the total mass.

NGC 2903 is considered an isolated galaxy, given the absence of nearby companions sufficiently massive to perturb it (No. 0347 in the Catalog of Isolated Galaxies; Karachentseva 1973). To date three small companions have been observed that are associated to NGC 2903 (Irwin et al. 2009), non of these are within the field of view of our data cube.

### 3.3.2 Velocity field

As described in section 3.2.1 we created the H I velocity field of NGC 2903 by fitting a Gaussian-Hermite to the velocity profiles. The field is presented in Figure 3.1b and shows typical disk-like kinematics. The velocity field has a warped appearance in both the approaching (North) and receding (South) side of the galaxy, as revealed by the increase in position angle at larger radii. The velocity field of NGC 2903 is slightly asymmetric and shows a shallower increase in velocity at the receding side than the approaching side does. Infall of substantial amounts of gas and stars can be the origin of the observed asymmetries in spiral galaxies (Ostriker & Binney 1989, Jiang & Binney 1999, Sancisi et al. 2008). It has to be noted though that apart from the asymmetry, warped structure, and lopsidedness no direct evidence of interaction with any of the close-by companions in the velocity field is seen.

### 3.3.3 Rotation curve

#### Methodology

The rotation curve of a galaxy can be derived using the velocity field, which shows the projected velocity along the line of sight at each position in the galaxy. For deriving the rotation curve of NGC 2903 we used a tilted ring method, using the ROTCUR package in GIPSY. We divided the galaxy in concentric rings, each with a width of 28 arcsec along the major axis. The first parameters to determine using the tilted-ring model are the systematic velocity of the galaxy and the dynamical centre. ROTCUR applies a least square fitting for every pixel in the ring to the function

$$v(x, y) = v_{\text{sys}} + v_{\text{rot}} \times \cos \theta \times \sin (INCL),$$

where  $v(x, y)$  is the projected velocity at position  $(x, y)$ ,  $v_{\text{sys}}$  is the systematic velocity of the galaxy,  $v_{\text{rot}}$  the rotational velocity and  $INCL$  is the inclination of the galaxy.  $\cos \theta$  is described

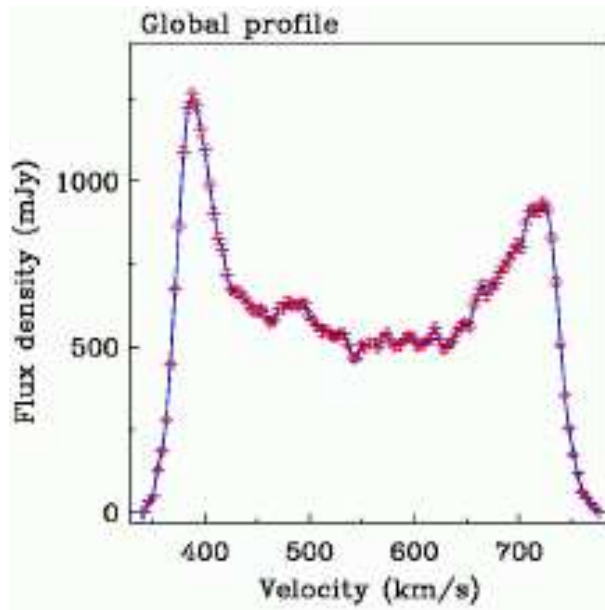


**Figure 3.2:** Global profile of NGC 2903

by:

$$\cos \theta = \frac{(x - XPOS) \times \sin(PA) + (y - YPOS) \times \cos(PA)}{r}$$

where XPOS and YPOS represent the dynamic centre of the galaxy, PA the position angle and  $r$  the distance to the dynamic centre. We neglect the contribution of expanding gas ( $v_{exp}$ ) in our calculations.

Our approach was as follows. We sampled the rotation curve every 5 arcsec using rings with a width of 28 arcsec with the dynamic centre, systematic velocity, position angle, and inclination of the galaxy left as variables. Radial velocities within 25 degrees around the minor axis were discarded in our calculations. In a first run we determined the systematic velocity and the dynamic centre. These were used as fixed input in the second run. We estimated the inclination from the second run using a running mean with a bin width of 20 arcsec and performed a third run with the estimated inclination as fixed input, together with the dynamic centre and systematic velocity. The position angle was then estimated in the same manner as the inclination, again using a running mean with a bin width of 20 arcsec. To obtain the rotation curve, a last run was performed with all the earlier estimated parameters as fixed input.

Apart from a rotation curve based on the entire galaxy, we obtained rotation curves based on the receding and approaching sides of the galaxy, with the aim of finding possible asymmetries. To do this correctly, we calculated the inclination and position angle for the entire galaxy, as well as for the receding and approaching sides.

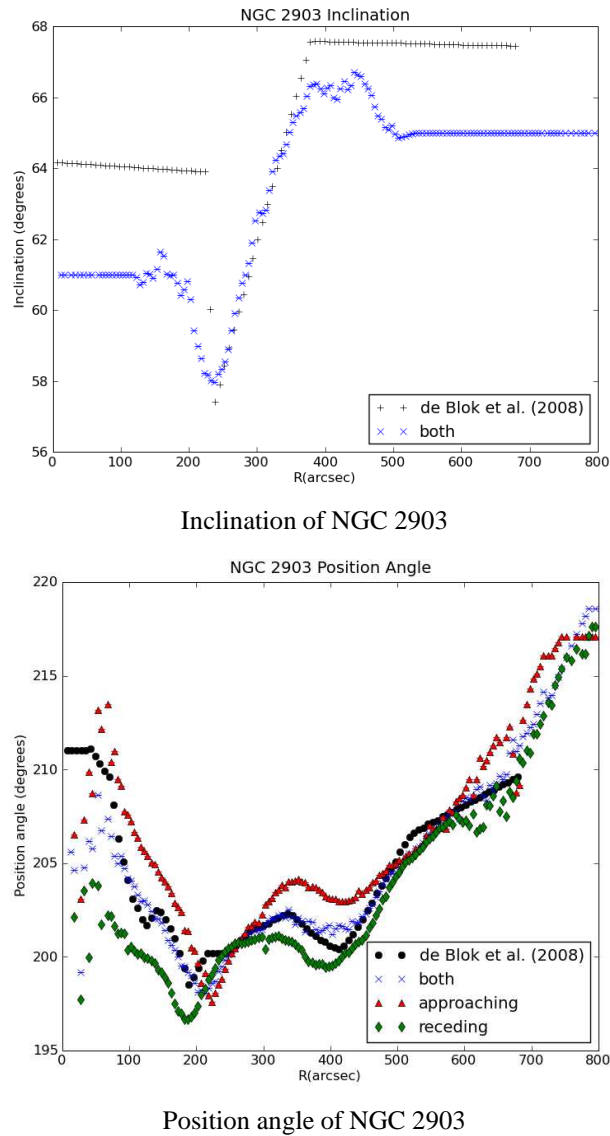


**Figure 3.3:** a) Change in inclination as a function of radius; b) Change in position angle as a function of radius. Blue crosses represent the position angle based on the entire galaxy. Red triangles the position angle based on the approaching side of the galaxy. Green diamonds represent the position angle based on the receding side of the galaxy.

### Parameters

From our first run we found a systematic velocity of  $V_{\text{sys}} = 556.4 \pm 1.2 \text{ km s}^{-1}$  which is in good agreement with  $V_{\text{sys}} = 557.3 \pm 1.3 \text{ km s}^{-1}$  by Begeman (1987) and  $V_{\text{sys}} = 555.6 \pm 1.3 \text{ km s}^{-1}$  by de Blok et al. (2008). We found the dynamical centre of NGC 2903 to be located at 9h32m10s +21h29m57s (J2000).

We found differences in inclination angle up to  $\sim 10$  degrees between the approaching and

receding sides of the galaxy at a radius of  $r \sim 110$  arcsec. This difference is associated with non-circular motions, corresponding to the outer radius of the spiral arms associated with the central bar. Similar evolution of the inclination with angle and correspondence with non-circular motions was observed by de Blok et al. (2008). Since the difference observed is the result of non-circular motions, we did not take these changes into account when calculating the NGC 2903 rotation curve. No other significant differences between the approaching and receding sides of the galaxy were found. We therefore used the estimate of the inclination angle based on the entire galaxy (Figure 3.3a) as fixed input for all remaining runs.

We fixed the inclination angle estimate used in the remaining runs to a constant value at low and high radii. Most of the datapoints in these regions have large errorbars due to low counts in the rings and influence by non-circular motions of the bar, which makes them unreliable. The fixed values represent the mean of the datapoints in these regions with small error bars ( $\sim 1$  degree). In between these regions there is a clear decrease followed by an increase in inclination angle. From the figure we see that our applied constant values for the inclination are slightly lower than the values applied by de Blok et al. (2008). We obtained a good fit for the variation of the inclination.

Position angles were calculated with the kinematic center, systematic velocity and inclination as presented in Figure 3.3a fixed. The estimated position angles for each side of the galaxy are presented in Figure 3.3b, with the de Blok et al. (2008) obtained position angle overplotted. We find that the position angles of the separate sides differ in amplitude in the inner region of the galaxy, and are similar in the outer region. Most striking is the phase shift between the position angle based on the approaching and receding side of the galaxy. There is a systematic offset of  $\sim 30$  arcsec ( $\sim 1.25$  kpc) between the two sides in the inner part of the galaxy, which suggests that the galaxy can not be considered fully axi-symmetric. The de Blok et al. (2008) position angle agrees well with our estimate of the position angle based on fitting the velocity field of the entire galaxy. The estimated position angles as presented in Figure 3.3b were used as fixed input in the final run of ROTCUR, to calculate the rotation curves.

## Result

We present the rotation curves of the receding and approaching side of the galaxy, and also the curve based on the entire galaxy in Figure 3.4. Overplotted is the rotation curve by de Blok et al. (2008). The rotation curves were calculated using the systematic velocity, dynamic center, inclination estimate as derived from the entire galaxy, and the position angle estimate of the side the corresponding rotation curve was based on as fixed input. In all our rotation curves we observe a steep increase in rotational velocity up to a maximum of  $210 \text{ km s}^{-1}$  at a radius of 140 arcsec. The curves decrease and then slightly increase to become almost flat, gradually decreasing to a value of  $185 \text{ km s}^{-1}$  at a radius of 650 arcsec.

We observe small systematic asymmetries in rotational velocities between the two sides of the

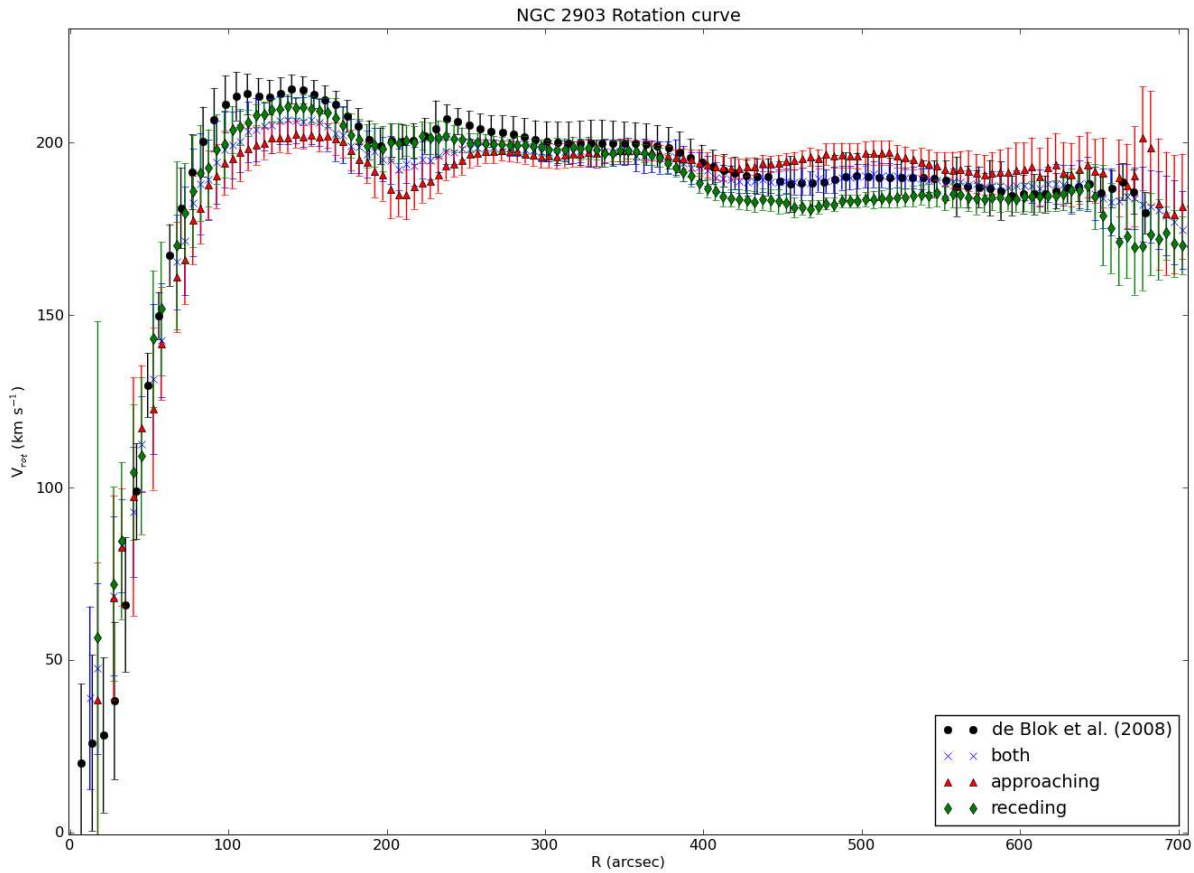


**Figure 3.4:** Comparison of our WHISP based rotation curve with the de Blok et al. (2008) rotation curve of NGC 2903. Black dots represent the de Blok et al. (2008) rotation curve; Blue crosses our rotation curve based on the entire galaxy; Red triangles our rotation curve based on the approaching side; Green diamonds our rotation curve based on the receding side of the galaxy.

galaxy. In the inner part of the galaxy ( $90 \lesssim r \lesssim 250$  arcsec) the receding rotational velocities are  $\sim 10 \text{ km s}^{-1}$  above the approaching rotational velocities, whereas it is the other way around in the outer region of the galaxy (at radii larger than  $\sim 390$  arcsec). It has to be noted that differences in velocity are all within the errorbars. The difference in amplitude and phase shift between the receding and approaching position angle can result in the differences observed in the inner region of the galaxy. The position angles are similar in the outer region of the galaxy and can not be the origin of the observed differences. The  $H\text{I}$  velocity field of the galaxy shows a slightly steeper increase in velocity with radius at the approaching side, than at the receding side. This asymmetry can result in the differences observed between the two sides in the outer part of the galaxy. We will get back to the origin of the asymmetry in rotation curve and the phase shift in the position angle between the separate sides of the galaxy in the discussion (Sec. 3.5)

The rise of the rotation curves agrees well with the rotation curve by de Blok et al. (2008). We find, within the errorbars, slightly higher rotational velocities in the inner 40 arcsec of the

galaxy. The integrated HI intensity field of NGC 2903 (Figure 3.1a) clearly shows the depletion of neutral gas in the central zone of the galaxy. Apart from this, our datacube has a lower resolution and therefore the inner most data points are based on just a few pixels. These two effects make the results in the most inner part of the galaxy somewhat uncertain.

Our rotation curve based on the entire galaxy is in fairly good agreement with the de Blok et al. (2008) results. We find rotational velocities slightly less than de Blok et al. (2008) in the region ranging from  $\sim 100$  to  $400$  arcsec. The difference in velocities observed is  $\sim 8 \text{ km s}^{-1}$  and within the errorbars. The agreement in the outer part of the galaxy between our rotation curve based on the entire galaxy and de Blok et al. (2008) is very good. Rotation curves based on the receding and approaching side of the galaxy mostly fall within the errorbars of de Blok et al. (2008). Only in the inner part of the galaxy ( $90 \lesssim r \lesssim 250$  arcsec) do we find our approaching rotation curve to be located below the de Blok et al. (2008) errorbars. Our estimate of the inclination angle in this part of the galaxy is less than the de Blok et al. (2008) estimate. However, it can not drive the differences observed between the rotation curves, since a decrease in estimated inclination angle will increase the rotational velocities calculated. Therefore, the origin of the observed difference in rotational velocity must be accounted to the velocity field of the approaching side of NGC 2903. Contrary to our results, de Blok et al. (2008) do not mention small asymmetries in rotation curves based on the approaching and receding sides of NGC 2903.

### 3.3.4 HI model velocity field and non-circular velocity maps

One of the main goals of this research is to study the link between the ionised gas kinematics and the ionised gas intensity (i.e. star-formation sites). In order to study the non-circular motions of the ionised gas we created a velocity field from the rotation curve and subtracted the model velocity field from the ionised gas velocity map. For reasons described later, we chose to create a model velocity field based on the HI rotation curve and not on an H $\alpha$  based rotation curve.

It is important to assure that only velocities due to rotation are subtracted (and not due to shocks, streaming motions etc.). It is difficult to get an exact separation of the two, but we made an approximation by smoothing the rotation curve with a running mean with a bin width of  $20$  arcsec. The model velocity field was made using the VELFI task, with the obtained smoothed rotation curve and the estimated inclination and position angle as input. The VELFI task creates a two dimensional velocity field given a systematic velocity, dynamical centre, rotation curve, inclination and position angle. We made three model velocity fields of NGC 2903 based on the rotation curve and position angle estimates of the entire, receding, and approaching sides of the galaxy. From these models three residual motion velocity maps, containing the non-circular motions, were created. HI non-circular velocity fields based on the entire galaxy, receding, and approaching sides of the galaxy are presentend in Figure 3.5, with indicative H $\alpha$  contours superimposed. The pixel size of the H $\alpha$  intensity map had to be degraded to the pixel size of the HI data.

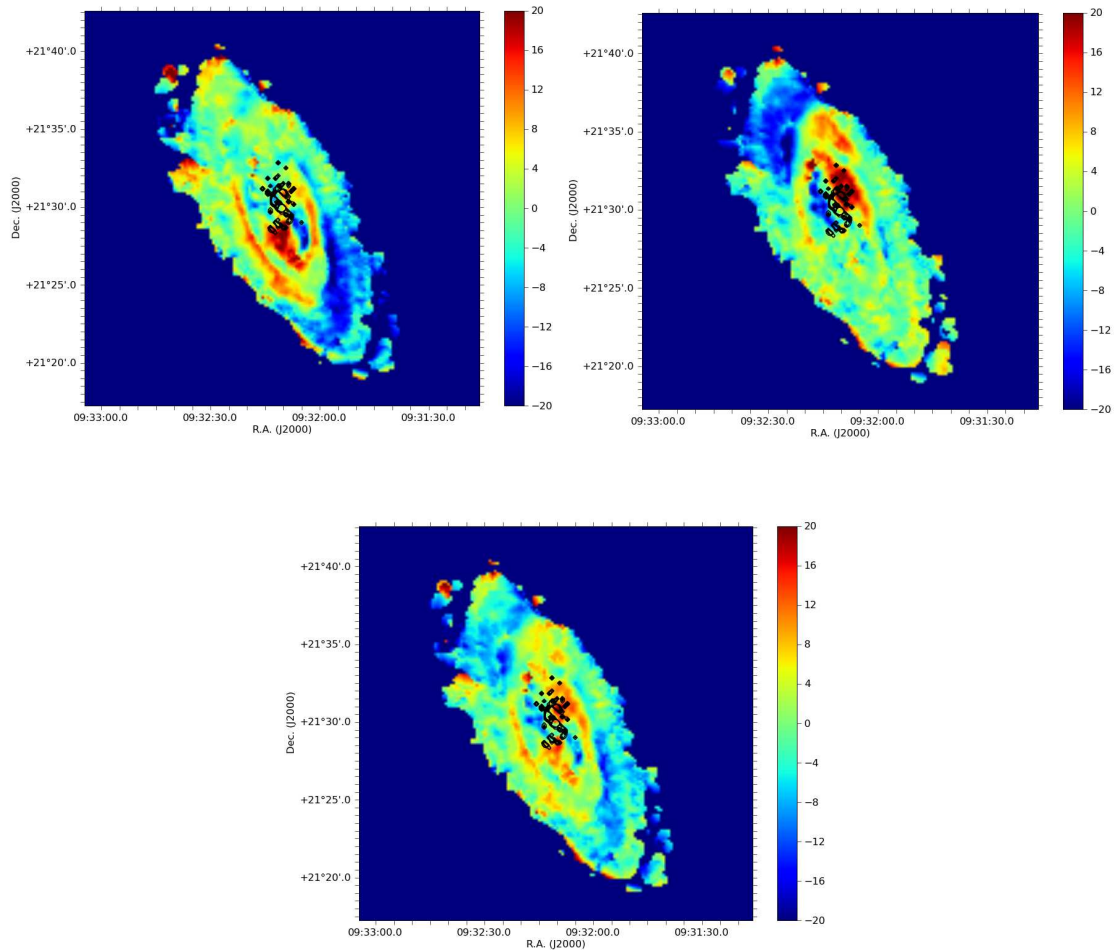


**Figure 3.5:**  $H\text{I}$  residual (non-circular) velocity map of NGC 2903. a) Residual map created using a model based on the approaching side; b) Residual map created using a model based on the receding side of the galaxy; c) Residual map created using a velocity model based on the entire galaxy. All velocities are in km/s.  $H\alpha$  contours are superimposed on both maps.

The quality of our velocity field models can be examined by carefully investigating the quality of our residual velocity fields. The residual velocities in the outer disk should be close to zero, if the rotation curve was determined correctly and the model velocity field created correctly. From Figure 3.5c one can immediately see the poor quality of the model velocity field based on the entire galaxy. Residual motions of  $\sim 10 \text{ km s}^{-1}$  are present throughout the galaxy. The model velocity field based on the separate sides of the galaxy show much better quality. The net residual motions of  $\sim 0 \text{ km s}^{-1}$  at the side of the galaxy corresponding to the side the model velocity field was based on, confirm that our applied measure of the systematic velocity is good. They also show that the model velocity fields are correct and do not contain signatures of a poorly chosen

dynamical centre.

The residual velocity maps clearly show the differences between the receding and approaching side of the galaxy. The map based on the receding side shows residual motions with a speed around zero at the receding side of the galaxy, with much larger residual motions at the approaching side and vice versa. This again clearly points out that the assumption of full axi-symmetry breaks down, as was already concluded from the asymmetry in the rotation curve and position angle.

We do not observe residual motions that can directly be linked to the infall of gas or a small object passing by. Especially the receding side of the galaxy has a very smooth residual velocity field. The inner part of the galaxy (containing the bar and the ring-like structure) shows small variations up to  $\sim 10 \text{ km s}^{-1}$  with some higher peaks. These velocities agree well with the residual motions of  $14 \text{ km s}^{-1}$  found by Trachternach et al. (2008).

More surprisingly, we do not see strong signs of the bar presence in the  $H\text{I}$  non-circular motions of NGC 2903. It has to be noted that the beam size of the  $H\text{I}$  data does not allow us to resolve the bar flow. Apart from this, Sellwood & Sánchez (2010) already suggested from the generally patchy and faint emission from neutral hydrogen in a sample of barred galaxies, that neutral hydrogen is a poor tracer of bar flows.

## 3.4 $H\alpha$ kinematics

In this section we will only discuss the  $H\alpha$  kinematics and how these might effect the star-formation in NGC 2903. The  $H\alpha$  morphology and others of NGC 2903 has been discussed in depth in a previous work (Popping et al. 2010).

### 3.4.1 $H\alpha$ velocity field

The intensity map and  $H\alpha$  velocity field of NGC 2903 are presented in Figure 3.6. We clearly see disk-like kinematics with some signs of gas response to a bar potential. Using a tilted-ring model we found a systematic velocity of  $V_{sys} = 556.1 \pm 1.1 \text{ km s}^{-1}$ , similar to the value obtained from the  $H\text{I}$  21 cm line. We found the kinematic centre to be located at 9h32m10s +21h30m01s (J2000).

There is a small enhancement in velocity ( $\sim 50 \text{ km s}^{-1}$ ) with respect to the surrounding in the knot at the end of the Northern side of the bar and to the East of the galaxy Nucleus. The large  $H\alpha$  emitting region just to the South of the nucleus has a velocity somewhat lower ( $\sim 50 \text{ km s}^{-1}$ ) than expected from the velocity field of a spiral galaxy. Same deviations of the spiral velocity pattern in NGC 2903 are present in the CO(1-0) transition-line velocity field of this galaxy (Helfer et al. 2003).

We note that several regions of  $H\alpha$  emission in the outer parts of the galaxy are missing in the

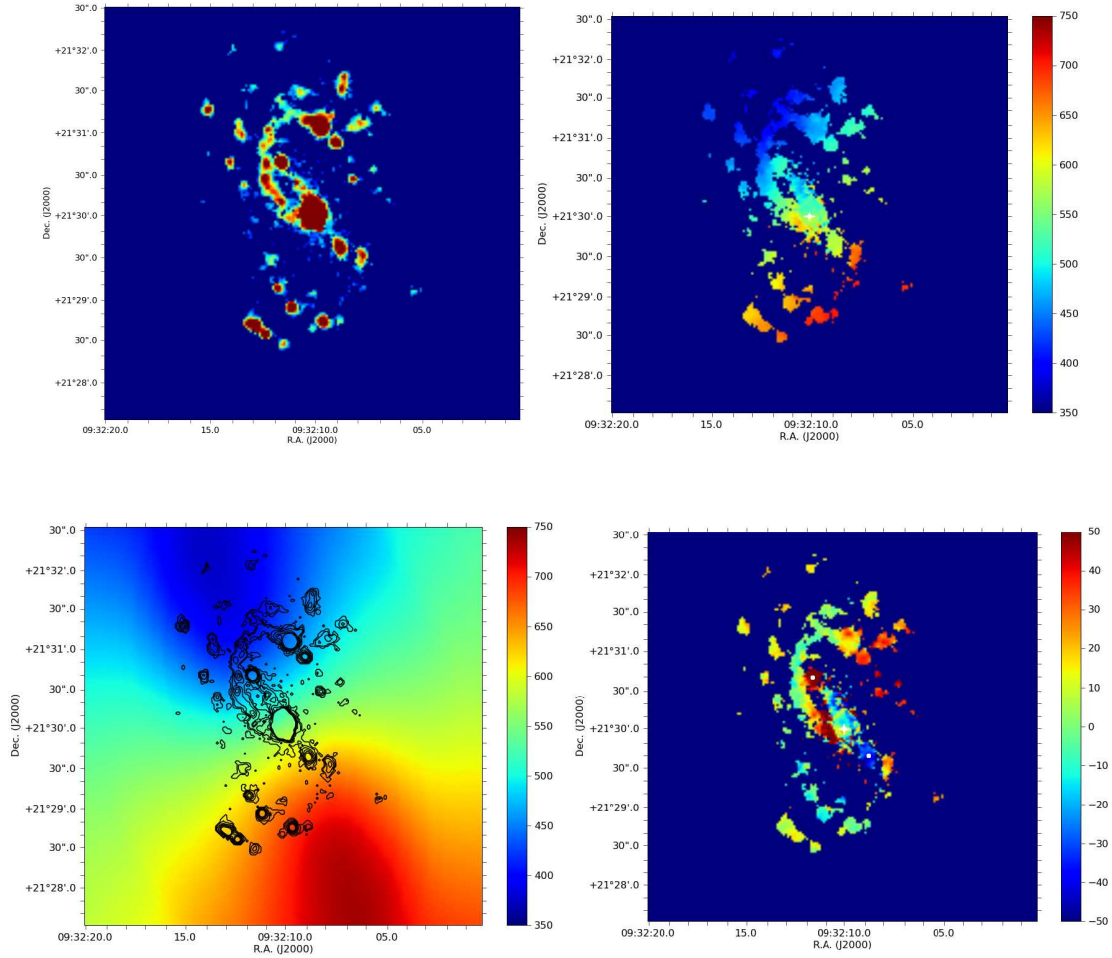


**Figure 3.6:** a)  $H\alpha$  intensity map of NGC 2903; b)  $H\alpha$  velocity field of NGC 2903 in km/s, the white cross represents the kinematic centre; c) Two dimensional projection model of the velocity field of NGC 2903 in km/s.  $H\alpha$  intensity contours are projected on top of the field; d) The  $H\alpha$  residual (non-circular) velocity field of NGC 2903 in km/s. The white cross represents the kinematic centre. The white dots are the two complexes with strong residual motions to the North and South of the nucleus the text refers to.

maps presented in this work. These regions emit their radiation at velocities outside the velocity range of the Fabry-Pérot interferometer and thus are not detected. As we restrict ourselves to the barred region of NGC 2903, this was no limitation for this project.

### 3.4.2 Ionised gas non-circular motions

We want to use the  $H\alpha$  data cube to study the link between the kinematics of the gas and star-formation in the bar by analysing the gas motions not due to circular rotation. Non-circular

motions from the observed velocity field were obtained by subtracting the 2-dimensional model, constructed from the H I based rotation curve.

We chose to use a model obtained using the H I because a) this model goes out to larger radii; b) this model is based on data covering a larger area and has smaller errors. We found the rotation curves based on the  $H\alpha$  and H I in our region of interest (up to 2 arcmin) to be similar, which justifies this choice.

We used the estimated inclination and position angle and smoothed rotation curve based on the entire galaxy as fixed input for VELFI. The model velocity field obtained thus is presented in Figure 3.6c. The bar area in both the receding and approaching H I residual velocity fields shows residual motions close to zero (see Figure 3.5). Differences in residual velocities in the bar between fields obtained by subtracting a velocity model based on the entire galaxy, and velocity models based on the receding and approaching sides, were found to be only minor. In the outer disk we found differences up to  $\sim 10 \text{ km s}^{-1}$ . This gave us confidence that the projection model based on the entire galaxy is suited for our aims. Furthermore, a model based on the entire galaxy was considered better suited for obtaining non-circular velocity profiles throughout the bar (Sec. 3.4.2).

The disadvantage of using a velocity field model based on the entire galaxy, is that it is hard for us to test the accuracy of the subtracted two dimensional velocity projection in the outer disk. Since the two sides of the galaxy show such large differences in rotation curve and position angle at larger radii, we do not expect net residual velocities of zero in the outer regions of the galaxy (apart from the complication that there is hardly  $H\alpha$  information in the outer regions of the galaxy). We can not examine the quality of the velocity model in the inner part of the galaxy either, since the residual velocity map will be dominated by gas response to the bar potential (i.e., streaming motions, shocks). We do observe residual motions centered around zero in the northern side of the bar though (see Sec. 3.4.2). Combined with the good quality of our H I residual maps, this gave us enough confidence on the good quality of our residual velocity map.

We did not include motions associated to the bar potential in our model velocity fields. Strong residual motions are therefore expected.

### **Ionised gas non-circular velocities in the bar**

A glimpse at the  $H\alpha$  residual velocities in NGC 2903 immediately shows the strong non-circular velocity knots at the Northern and Southern side of the bar (indicated with white dots), as well as to the East of the galaxy nucleus (Figure 3.6d). The knots at the Northern and Southern bar sides are located symmetrically with respect to the nucleus, with receding velocities up to  $\sim 50 \text{ km s}^{-1}$  at the Northern side and similar approaching velocities at the Southern side. The signs of strong non-circular velocities are already visible in the  $H\alpha$  velocity field of the galaxy and the velocity field based on CO(1-0) observations (Helfer et al. 2003). The complex to the East of the galaxy nucleus is somewhat elongated and has receding non-circular velocities up to  $\sim$

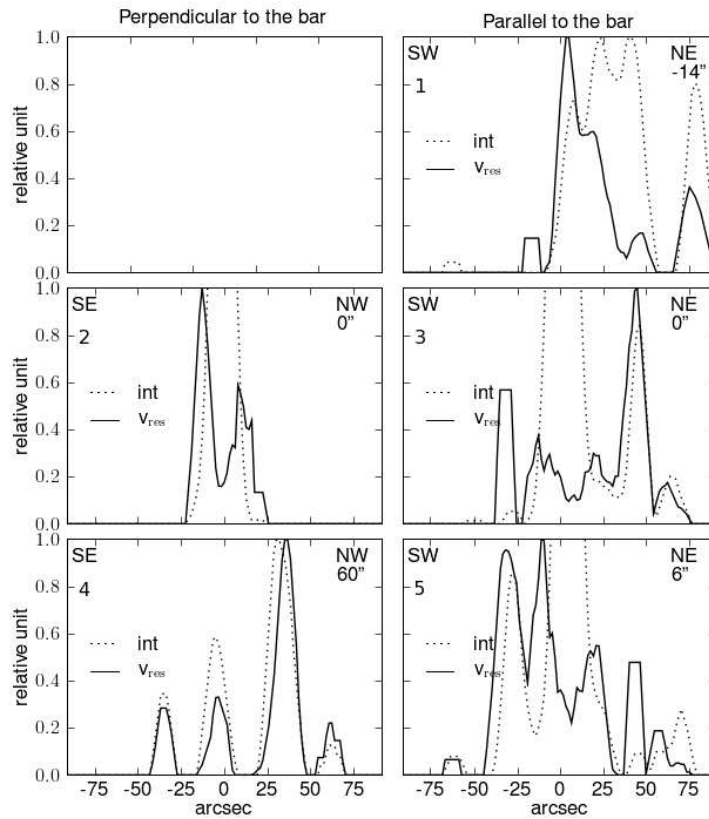


**Figure 3.7:** Profiles of the normalized  $H\alpha$  surface brightness and normalized absolute residual velocity. Positive distances in the profiles perpendicular and parallel to the bar are respectively to the NW and NE. Numbers in the upper left corner of each panel correspond to the label of each profile in Figure 3.8.

$80 \text{ km s}^{-1}$ . This complex has no counterpart at the Western side of the galaxy nucleus. The little amount of CO(1-0) present at this location does not show signs of prominent non-circular motions (Helfer et al. 2003).

Apart from these three complexes we do not observe strong non-circular motions in the bar (i.e., non-circular motions are centered around zero). Enhancements in non-circular motions up to  $\sim 25 \text{ km s}^{-1}$  are observed around  $H\text{II}$  regions. We will discuss these in Sec. 3.4.2. The ionised gas in the nucleus has non-circular velocities varying between about  $-15$  and  $15 \text{ km s}^{-1}$ .

Our results are in good agreement with the non-circular motions found in  $H\alpha$  by Sellwood & Sánchez (2010). The authors found velocities for the strong non-circular motion complexes to the North, South and East of the galaxy nucleus similar to our findings. In the remaining of the bar region they found non-circular motions centered around zero with enhancements up to  $20 \text{ km s}^{-1}$ , which also agrees with our results.

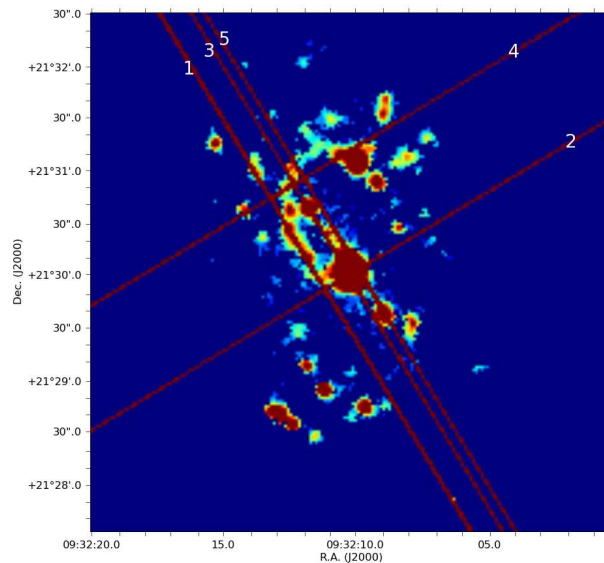


**Figure 3.8:**  $H\alpha$  intensity map of NGC 2903 with the location at which profiles were taken on top of them. The labeling of each profile corresponds to the profiles presented in Figure 3.7.

### Non-circular motions vs. $H\alpha$ intensity

The interplay between ionised gas non-circular velocities and intensity can occur on two different scales; 1) Global scale relations which extend over the entire bar and are driven by the gas response to the bar potential; 2) Local scale relations around H II regions like gas in- and outflow.

With the aim of studying the links between the star-formation in the bar to surrounding kinematical features, we obtained cross sections perpendicular and parallel to the bar of the non-circular velocity map, and compared these to their corresponding  $H\alpha$  intensity profiles. We selected the locations of the profiles manually, such that they would encompass as much emission as possible in a fair sampling of the bar. The profiles and their location in the galaxy are presented in Figures 3.7 and 3.8 respectively. Positive distances in the profiles perpendicular and parallel to the bar are respectively to the NW and NE. To overcome scatter in the  $H\alpha$  intensity and non-circular velocities, we applied a running mean with a bin width of 5 pixels (i.e., 8 arcsec) to the profiles.

In most profiles we observe that peaks in intensity and non-circular velocities are shifted  $\sim 3$  arcsec ( $\sim 125$  pc) from each other. A similar trend is observed around the nucleus of the galaxy with a shift of  $\sim 12.5$  arcsec. These shifts reflect a relation between ionised gas non-circular motions and intensity on a local scale. The upper right panel of Figure 3.7 shows strong  $H\alpha$  intensity without strong non-circular motion counterpart on a more global scale. However, peaks in ionised gas intensity and non-circular velocities do overlay. This profile does not demonstrate an interplay such, that strong non-circular motions are anti-correlated with peaks in intensity or vice versa. From the profiles we do not observe global relations between ionised gas intensity and non-circular motions.

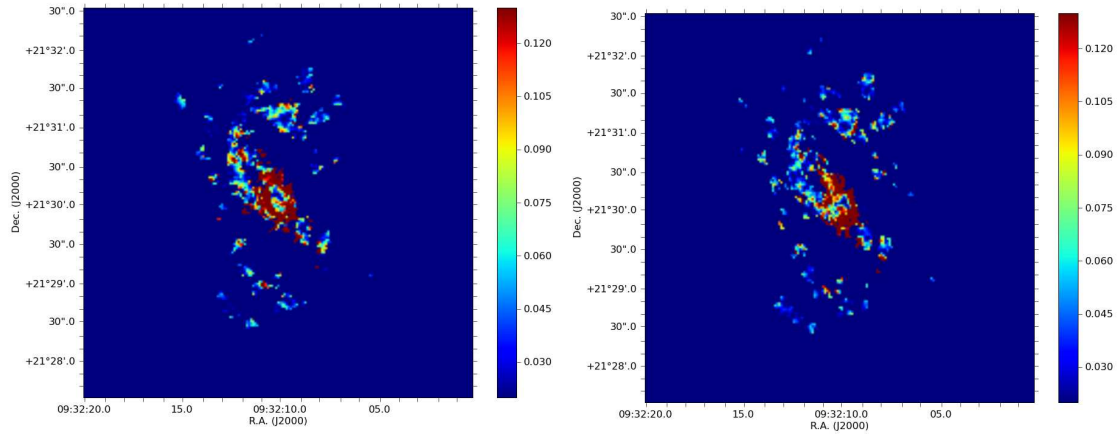


**Figure 3.9:** a) Perpendicular oriented  $H\alpha$  velocity gradient field of NGC 2903; b) Parallel oriented  $H\alpha$  velocity gradient field of NGC 2903. Velocity gradients are in  $\text{km s}^{-1} \text{pc}^{-1}$

We zoomed in on several  $H\text{II}$  regions, as it might allow us to determine what process causes the small shifts observed between peaks in ionised gas non-circular motions and intensity. The best region to observe this local interplay is just to the North of the fast receding non-circular motion complex East to the galaxy nucleus. This is the only clear barred complex visible in  $H\alpha$  in this galaxy and a very representative region to examine in depth, since it fits with our main goal to achieve insight in the link between kinematics and star-formation in bars.

Regions of strong  $H\alpha$  emission in this area of the bar are located in regions with low residual velocities (only a few  $\text{km s}^{-1}$ ), with stronger non-circular motions nearby them. Shifts are similar to what we saw in the profiles. The strong  $H\alpha$  emitting regions at the end of the 'S' shape at the Northern side of the galaxy nucleus shows similar behaviour. The centre of the  $H\text{II}$  region is located at a region with lower residual velocities than its surrounding. Clearly the residual velocity increases at the edge of the  $H\text{II}$  regions.

Regions of the galaxy dominated by strong non-circular motions (i.e; to the North and South of the galaxy nucleus (see the marks in Figure 3.6d, as well as to the East)) show the same trend. We found variations in the non-circular motions such, that the peak in  $H\alpha$  intensity is located in a trough of the non-circular velocity and the motions become more prominent at the edge of the  $H\text{II}$  regions. The non-circular velocity dominated regions to the North and South of the galaxy nucleus are among the brightest  $H\text{II}$  regions in the bar. The region to the East of the galaxy nucleus is not so bright.

### 3.4.3 $H\alpha$ velocity gradients

Gradients in the non-circular velocity map can give more insight in the location of shocks and shear in the bar, and how these enhance or inhibit the star-formation on a global scale. We created velocity gradient maps in the direction parallel and perpendicular to the bar, to achieve as many information about the gas flows induced by the bar potential. Perpendicular gradients trace shear in the bar at locations where two flows with different directions pass each other. Parallel gradients trace shocked regions that suddenly speed up the gas. Although gradients parallel and perpendicular to the bar are not perfect representations of shocks and shear, they are a good and easy way to approximate them.

Non-circular velocity gradient fields in a given direction were created using the method presented in Zurita et al. (2004). The residual velocity map was displaced by one pixel in that direction and subtracted from the original map. The same procedure was performed in the opposite direction. The velocity gradient map was obtained by adding the two newly created maps and dividing them by 2. For the pixels at the edge of the galaxy (for which subtracting with a neighbouring pixel means subtracting with a blank pixel) the displacement was carried out in only one direction. This procedure was carried out both perpendicular and parallel to the bar, which resulted in two velocity gradient maps of NGC 2903. The produced gradient maps are presented in Figure 3.9.

The majority of the  $H\alpha$  emission in both the Northern and Southern side of the bar has non-circular velocity gradients slightly larger than zero. We observe some perpendicular and parallel velocity gradient enhancements mostly in the range between  $0.06$  and  $0.10 \text{ km s}^{-1} \text{ pc}^{-1}$ , with some higher velocity gradient peaks of  $\sim 0.12 \text{ km s}^{-1} \text{ pc}^{-1}$ . The nucleus of NGC 2903 contains large fractions of ionised gas with both perpendicular and parallel velocity gradients of  $\sim 0.3 \text{ km s}^{-1} \text{ pc}^{-1}$  even up to twice this amount. The gradients in the nucleus reflect the changes in non-circular motions within the nucleus of NGC 2903, together with the region East to the galaxy nucleus with strong receding non-circular motions.

The velocity gradients in the bar are a factor 2-3 less than the  $H\alpha$  velocity gradients observed in the bar of NGC 1530 (Zurita et al. 2004). Our strongest velocity gradients in the bar measure up with the weakest velocity gradients in the NGC 1530 bar. The velocity gradients observed in the nucleus of NGC 2903 are slightly stronger than the velocity gradients in the nuclear region of NGC 1530. NGC 1530 though, does not show the strong variations in the non-circular motions within the galaxy nucleus as NGC 2903 does.

Because of the lack of strong non-circular velocity gradients in the bar of NGC 2903, we only briefly looked at its interplay with  $H\alpha$  intensity. We found 'stronger' velocity gradients to be located at the edges of H II regions compared to the gradients within the H II regions. This behaviour is similar to what we observed for the relation between  $H\alpha$  non-circular velocity and intensity on local scales.

Zurita & Pérez (2008) found a spatial correlation between parallel oriented velocity gradients

and dust spurs at the trailing side of the galaxy. We did not search extensively for such a trend. Firstly because of a lack of H $\alpha$  emission at the trailing side of the bar and a lack of strong velocity gradients. Secondly, because a quick look did not reveal a trend between dust spurs and filaments in the bar, apart from dust depletion on top of H II regions corresponding spatially with extremely weak velocity gradients.

### 3.5 Discussion

NGC 2903 was always considered a typical strong bar classified in the NIR with a bar strength of 3 (Laurikainen & Salo 2002). In a previous paper we already argued that the broken and wide structure of the dust lanes, combined with the different morphological appearances in different wavelength bands, might be evidence that the bar is not so strong. In this paper we obtained ionised gas velocity gradients oriented both parallel and perpendicular to the bar, and non-circular velocities in the bar as a measure of the shock strengths and found velocity gradients and non-circular motions 2-3 times as weak as in NGC 1530. Furthermore, the gradients are not as closely aligned with the dust lanes in the bar. These results put a question mark to the measured strength of this bar, or at least suggest that strong bars as measured from broad-band imaging do not necessarily imply the occurrence of strong shocks.

These results should be of interest to those who model bars. Athanassoula (1992) found that the shock strength and location, as traced by dust lanes, are strongly dependent on the strength of the bar, with strong bars containing strong shocks and straight dust lanes along their bar major axis. The bar strength in the Athanassoula (1992) models was determined using the bar axis ratio and mass of the bar. Our results show that bars which are considered to be strong as determined using broad-band measurements, do not necessarily show the dynamics as predicted by the models for strong bars.

Three regions of strong ionised gas non-circular motions are present in the NGC 2903 bar. The symmetric location of the strong non-circular motion complex to the North and South of the galaxy nucleus, their similar values, and their location with respect to the bar major axis suggest that these complexes are most likely due to the elliptical orbits of the gas in the bar. The velocities observed are in good agreement with suggested streaming motions of 50-80 km s<sup>-1</sup> obtained from CO observations, and streaming motions found using HCN(1-0) as kinematic tracer of the gas (Léon et al. 2008). Sellwood & Sánchez (2010) argue that the high velocities reflect bar induced streaming motions. A proper hydrodynamic model of the gas in the bar would be necessary to confirm that the regions we find to the North and South are indeed part of the bar flow streaming motions, but this is beyond the scope of this study.

The non-circular complex to the East of the galaxy nucleus matches with the highest observed streaming motions using CO as the kinematic tracer (Léon et al. 2008), but has no symmetric counterpart at the other side of the nucleus. This complex could also be associated to the bar

flow, however, this is not as straight forward as for the other high non-circular velocity regions. A major part of the region has a UV stellar age much older than the other stars in the bar and is located close to the large UV complex with no  $H\alpha$  nor  $24\ \mu\text{m}$  emission to the southeast of the nucleus (Popping et al. 2010). We concluded that these regions are not linked to the bar potential. From the coincidence of the  $H\alpha$  emitting region to the East of the nucleus with the older UV complexes, one could argue that the ionised gas is not linked to the bar potential and that the observed velocities are not due to bar induced flows.

From  $H\alpha$  non-circular motions and  $H\alpha$  surface brightness profiles we observe a small shift of  $\sim 3$  arcsec ( $\sim 125$  pc) between peaks in residual velocity and brightness in  $H\text{II}$  regions. This shift is also observed directly from the residual velocity and intensity maps, with the non-circular motions being stronger at the edge of the  $H\text{II}$  regions. Zurita et al. (2004) present three phenomena that will lead to this result on local scales (whether combined or not); 1) The first is the effect of the elliptical orbits on the condensation of molecular clouds. The presence of strong shear should act against the condensation of massive gas clouds, thus preventing the formation of stars; 2) Strong shocks in bars are expected to be regions where the global motion of the elliptical orbits is strongly braked and star-formation is accelerated (Elmegreen et al. 2002). This will result in regions with only small non-circular velocities and strong star-formation; 3) Stellar winds of young stars can blow the surrounding gas away, thus creating strong non-circular motions around  $H\text{II}$  regions. Unfortunately, from our set of observations we are not able to pin down the physical process that determines the shape of our profiles.

One of our aims was to study the interplay between kinematics and star-formation for the case of NGC 2903 and put this into the context of the discrepancy between star-formation locii in the bar of NGC 2903 and the hypothesis by Sheth et al. (2000, 2002). The authors proposed that stars form at the trailing side of the major bar dust lane, and migrate towards the leading side as they age, however, no such trend is observed in NGC 2903 (Popping et al. 2010). A study on NGC 1530 (which was found to be in good agreement with the Sheth et al. (2000, 2002) hypothesis; Zurita & Pérez 2008) revealed a strong anti-correlation between the non-circular motions and  $H\alpha$  surface brightness profiles on a global scale of tens of arcsec (Zurita et al. 2004). No such anti-correlation was found in NGC 2903, only minor shifts between the two profiles on local scales.

The potential of a bar will determine the position and strength of shocks and the relation between non-circular motions and star-formation. From wide broken dust lanes, complex morphology and the weak ionised gas velocity gradients we already suggested that the NGC 2903 bar is not as strong as measured from broad-band imaging. The lack of anti-correlation between non-circular motions and star-formation as observed in strong bars, and the star-formation locii and evolution not fitting in with the hypothesis suggested by Sheth et al. (2000, 2002), suggest that these processes are not strongly driven by the bar potential. This emphasises our finding that NGC 2903 might not be as strong as was thought from broad-band imaging.

The  $H\text{I}$  neutral gas distribution, as well as the velocity field, shows several features that point

towards an encounter with a small companion, or at least a small companion passing by. The distribution of the neutral gas has a warped and lopsided structure. It was argued by several authors that both events can have the infall of substantial amounts of gas and stars as their origin (Ostriker & Binney 1989, Jiang & Binney 1999, Sancisi et al. 2008).

The H I residual velocity maps clearly exhibit differences between the receding and approaching side of the galaxy. Systematic and symmetric deviations from circular orbits are present at the side of the galaxy for which the corresponding velocity model was not based on. The origin of this deviation can be accounted to the position angle. This is clearly demonstrated by the change in position angle with radius between the separate galaxy sides. Apart from differences in amplitude of the position angle, we found a systematic phase shift of 30 arcsec between the two sides of the galaxy. The rotation curve of NGC 2903 also demonstrates asymmetry between the approaching and receding sides of the galaxy. All these results clearly point out that the hypothesis of axi-symmetry breaks down for NGC 2903. Although not directly observed, it is most likely that some external object disrupted the dynamics of the gas resulting in the asymmetries and phase-shift observed.

The rearrangement of the NGC 2903 gas dynamics by an external origin is important in the context of gas dynamics in the bar and the hypothesis on star-formation in bars as proposed by Sheth et al. (2000, 2002). It suggests that the dynamical weakness of the bar and the observed star-formation behaviour in NGC 2903 are the result of a small encounter, and not secular evolution. The interaction with an external object is also of great importance in understanding the presence of UV knots in a spiral like distribution perpendicular to the bar, with no significant amount of H $\alpha$  and 24  $\mu$ m emission, and ages much older than the remaining knots. We proposed a small merger event inducing a star burst as a possible hypothesis for the origin of these knots.

### 3.6 Summary and Conclusion

We have carried out a detailed study of the kinematics of the neutral and ionised gas content of NGC 2903, and how these are linked to the star-formation in the galaxy. We obtained the rotational velocity, inclination and position angle from the H I as a function of radius and analysed the distribution of the neutral gas. We created a model velocity field and used this to obtain H I and H $\alpha$  non-circular velocity fields. We have compared the H $\alpha$  non-circular velocity field and H $\alpha$  intensity map and created profiles of these through the bar of the galaxy. Furthermore, we have obtained a map of the ionised gas velocity gradient in the bar zone. Our main results are:

- NGC 2903 exhibits a velocity field typical for a disk galaxy, both in the H I and H $\alpha$ . We find non-circular motions in the H I up to  $\sim 10 \text{ km s}^{-1}$ , and in the H $\alpha$  up to  $\sim 25 \text{ km s}^{-1}$  with enhancements up to  $\sim 50 \text{ km s}^{-1}$  due to streaming motions in the bar. The non-circular velocities are within typical ranges and in good agreement with previous observations.

- There is a shift of  $\sim 3$  arcsec ( $\sim 125$  pc) between peaks in  $H\alpha$  intensity and non-circular velocity profiles. These peaks mark the increase of non-circular motions outwards H II regions. No global relation between ionised gas non-circular motions and intensity other than that the two overlay is observed in the bar.
- The NGC 2903 bar does not show the typical features associated to strong bars. This is demonstrated by the broken wide structure of dust lanes, lack of strong gradients and shocks. These results suggest that although NGC 2903 is classified as strong using broad-band imaging, the dynamics point to a weaker bar.
- The galaxy has a warped and lopsided neutral gas distribution with a mass of  $(48.00 \pm 0.04) \times 10^8 M_{\odot}$ .
- The H I velocity field reveals a clear asymmetry between the receding and approaching side of the galaxy. The rotation curve is asymmetric, a systematic phase shift is present in the position angle as a function of radius between the two galaxy sides, as well as difference in amplitude in the inner region. The H I non-circular velocities also demonstrate the large difference in position angle between the receding and approaching side.

These results point out that NGC 2903 probably met a small companion that rearranged the dynamics of the galaxy. It suggests that the lack of typical features associated to strong bars and star-formation behaviour in the NGC 2903 bar are the result of this small encounter, and not secular evolution. It is likely that the encounter has to do with the origin of the UV complexes with significant amount of neither  $H\alpha$  nor  $24 \mu\text{m}$  wavelength emission. However, information of the stellar motions in this regions would be necessary in order to shed light on the detailed origin. Furthermore, deep H I observations could reveal the presence of weak H I complexes associated to a merger event.

The results also point out that broad-band measures might not be sufficient to determine the strength of a bar, or at least are not sufficient to predict the dynamical behaviour of the gas in the bar.

## Acknowledgements

G. Popping acknowledges support by the Stichting Groninger Universiteitsfonds. I. Pérez & A. Zurita acknowledge support from the Spanish Plan Nacional del Espacio de Ministerio de Educación y Ciencia (via grant C-CONSOLIDER AYA 2007-67625-C02-02). I. Pérez & A. Zurita also thank the Junta de Andalucía for support through the FQM-108 project. We would like to thank Mónica Relaño for useful discussions and Erwin de Blok and Olivier Hernandez for providing us with data.



---

# Conclusion and future work

The work carried out in this thesis is aimed at understanding the processes that drive star-formation in the strongly barred spiral NGC 2903. The emerged idea on star-formation in bars states that stars form at the trailing side of the bar major dust lane and migrate towards the leading side. The spatial distribution of star-forming sites and their age in NGC 2903 does not correlate with any morphological feature of the bar.

This result, different morphologies in different wavelength bands, the patchy spiral shape morphology of NGC 2903 as revealed by the UV, combined with the broken wide dust lanes, suggest that NGC 2903 is dynamically very complex. This is emphasised by a spiral shape distribution of UV knots perpendicular to the bar, with significant amount of neither  $H\alpha$  nor  $24\ \mu\text{m}$  wavelength emission. These complexes have stellar ages much older than the other UV knots in the galaxy, and are regions currently not favoured by the bar potential to form stars. These results demonstrate that the dynamics of a galaxy is essential to understand where and when star-formation is triggered.

$H\alpha$  kinematics indicate that NGC 2903 does not show the typical features associated to strong bars. The bar has a lack of strong gradients, shocks, and non-circular motions. Interplay between  $H\alpha$  non-circular motions and intensity does only seem to play a role at  $H\text{II}$  region scales, not at larger scales as observed in NGC 1530. It suggests that star-formation is not strongly driven by the bar potential, also indicated by a lack of correlation between the spatial distribution of star-formation sites and ages with bar morphological features. All these observations, combined with the broken wide dust lanes and complex morphology, suggest that the NGC 2903 bar might just not be as strong as was suggested from broad-band imaging. It implies that broad-band imaging might not be sufficient to determine the actual strength of a bar.

The  $H\text{I}$  distribution and velocity field contain several signs of a recent minor-merger event. The galaxy is warped, lopsided, and rotational velocities and position angle as a function of radius have a non-axisymmetric appearance. Such a minor-merger event is likely to be the origin of the complex morphological and dynamical appearance, or a weaker bar than suggested from broad-band imaging in general. It suggests that the observed properties of NGC 2903 are not the result of secular evolution.

In the future deep  $H\text{I}$  observations would be necessary to find direct evidence of a recent merger event. Combined with stellar velocity information this would give us a complete dynamical picture of this complex barred spiral. A complete picture will be necessary to obtain insight

in the underlying dynamics of the spiral shape UV complexes perpendicular to the bar.

If NGC 2903 indeed recently was subject of a minor merger event, it can serve as an ideal object to study the implications of such an event on barred galaxies or possibly disk galaxies in general; Is the bar weaker than suggested from broad-band imaging because the merger event rearranged the bar gas dynamics, or is the bar a result of the merger event and maybe even still in formation?; How do gas and stars react to the formation or disruption of a bar?; What does the dynamical behaviour of the material traced by different wavelength bands look like and how are these related to a merger event?; etc.

In order to understand the processes that drive star-formation along bars we would need to have a larger sample of barred spirals. An important aspect of this sample is the strength of the bar, as it will drive the gas dynamics and star-formation. Although broad-band imaging can serve as a good indicator of bar strength, clearly it is not always a good representation of the actual bar potential. A new way of defining bar strength, including features like; patterns of the dust lanes; strength of the velocity gradient; morphological appearance in multiple wavebands, might result in measures of bar strength closer to the real bar potential. Especially velocity gradients can serve as a good direct indicator of the actual strength of a bar.

---

# Acknowledgements

This project goes back a long time, starting October 2007. It was then that I came in touch with Isa, carried out the  $H\alpha$  observations of NGC 2903 for a bachelor course, and started working on my bachelor thesis (which evolved into my masters thesis). Since then, I have learned many things and there are a few persons that significantly contributed to the final result of this thesis.

First of all, I would like to thank Isa, my main supervisor. Thank you for all the nice times we had during the last two years and coming home safely after every dangerous trip. You have become my scientific mother, learning me the beginnings of doing science, being precise and guiding me through all the struggles that we encountered. I am glad you always remained enthusiastic, made me take wrong decisions and let me deal with them until I realised I was wrong myself. I appreciate your hospitality and a big thanks to you and Angel for taking me on my first outdoor skiing trip. I will always look back at the Maria devotion as one of my most remarkable experiences in my live.

Dear Almudena, thank you for always being there at the other side of the screen during skype meetings. You always gave quick and clear answers to my questions regarding  $H\alpha$  kinematics,  $H\text{ II}$  regions, and others, which helped me a lot. In Granada you usually were the first person I talked to in the morning and it always felt like a warm welcome at the institute.

I would also like to thank Thijs, my supervisor in Groningen. Although you have a full schedule, I could not have wished for a better supervisor. You made plenty of time for me and your experience and knowledge of  $H\text{ I}$  and datacubes made the last half year much easier.

Thank you Monica for providing me with the  $H\alpha$  interferometric data and helping me reducing it. Thanks Wim for all the times you set up GAIA and the interesting talks we had.

I am lucky with the great group of students at Kapteyn. You all helped; either by answering questions on programming or science issues, or by accompanying me during necessary breaks.

I want to thank my family for their support and interest. A last big thanks to Anke. You always forced me to come up with the strangest comparisons in order to explain the progress and outcomes of my thesis. It often gave me a clearer picture of my work and for sure made me realise how beautiful astronomy is. Thank you for always supporting me, for all the fun we have together and being my buddy in everything. I'm glad to have you by my side!



---

## Bibliography

- Alonso-Herrero, A., Ryder, S. D. and Knapen, J. H.: 2001, Nuclear star formation in the hotspot galaxy NGC 2903, *MNRAS* **322**, 757–769.
- Athanassoula, E.: 1992, The existence and shapes of dust lanes in galactic bars, *MNRAS* **259**, 345–364.
- Athanassoula, E.: 2000, Gas Flow in Barred Galaxies, in D. Alloin, K. Olsen, & G. Galaz (ed.), *Stars, Gas and Dust in Galaxies: Exploring the Links*, Vol. 221 of *Astronomical Society of the Pacific Conference Series*, pp. 243–+.
- Beck, R.: 2002, Magnetic Fields in Spiral Arms and Bars, in E. Athanassoula, A. Bosma, & R. Mujica (ed.), *Disks of Galaxies: Kinematics, Dynamics and Perturbations*, Vol. 275 of *Astronomical Society of the Pacific Conference Series*, pp. 331–342.
- Begeman, K. G.: 1987, PhD thesis, , Kapteyn Institute, (1987).
- Bianchi, L. and Efremova, B. V.: 2006, The Recent Star Formation in NGC 6822 from Hubble Space Telescope Imaging, *AJ* **132**, 378–392.
- Bianchi, L., Madore, B., Thilker, D., Gil de Paz, A. and GALEX Science Team: 2003, The GALEX Nearby Galaxies Survey, *Bulletin of the American Astronomical Society*, Vol. 35 of *Bulletin of the American Astronomical Society*, pp. 1354–+.
- Bianchi, L., Thilker, D. A., Burgarella, D., Friedman, P. G., Hoopes, C. G., Boissier, S., Gil de Paz, A., Barlow, T. A., Byun, Y.-I., Donas, J., Forster, K., Heckman, T. M., Jelinsky, P. N., Lee, Y.-W., Madore, B. F., Malina, R. F., Martin, D. C., Milliard, B., Morrissey, P., Neff, S. G., Rich, R. M., Schiminovich, D., Siegmund, O. H. W., Small, T., Szalay, A. S., Welsh, B. Y. and Wyder, T. K.: 2005, Recent Star Formation in Nearby Galaxies from Galaxy Evolution Explorer Imaging: M101 and M51, *ApJ* **619**, L71–L74.
- Bresolin, F. and Kennicutt, Jr., R. C.: 1997, UBV<sub>R</sub> and H( $\alpha$ ) Photometry of H II Regions and OB Associations in Galaxies: A Test for a Variable IMF, *AJ* **113**, 975–980.
- Calzetti, D.: 2001, The Dust Opacity of Star-forming Galaxies, *PASP* **113**, 1449–1485.

- Calzetti, D., Armus, L., Bohlin, R. C., Kinney, A. L., Koornneef, J. and Storchi-Bergmann, T.: 2000, The Dust Content and Opacity of Actively Star-forming Galaxies, *ApJ* **533**, 682–695.
- Calzetti, D., Kennicutt, Jr., R. C., Bianchi, L., Thilker, D. A., Dale, D. A., Engelbracht, C. W., Leitherer, C., Meyer, M. J., Sosey, M. L., Mutchler, M., Regan, M. W., Thornley, M. D., Armus, L., Bendo, G. J., Boissier, S., Boselli, A., Draine, B. T., Gordon, K. D., Helou, G., Hollenbach, D. J., Kewley, L., Madore, B. F., Martin, D. C., Murphy, E. J., Rieke, G. H., Rieke, M. J., Roussel, H., Sheth, K., Smith, J. D., Walter, F., White, B. A., Yi, S., Scoville, N. Z., Polletta, M. and Lindler, D.: 2005, Star Formation in NGC 5194 (M51a): The Panchromatic View from GALEX to Spitzer, *ApJ* **633**, 871–893.
- Cedr s, B., Cepa, J. and Tomita, A.: 2005, Comparison of the  $H\alpha$  Equivalent Width of H II Regions in a Flocculent and a Grand-Design Galaxy: Possible Evidence for Initial Mass Function Variations, *ApJ* **634**, 1043–1055.
- Dale, D. A., Cohen, S. A., Johnson, L. C., Schuster, M. D., Calzetti, D., Engelbracht, C. W., Gil de Paz, A., Kennicutt, R. C., Lee, J. C., Begum, A., Block, M., Dalcanton, J. J., Funes, J. G., Gordon, K. D., Johnson, B. D., Marble, A. R., Sakai, S., Skillman, E. D., van Zee, L., Walter, F., Weisz, D. R., Williams, B., Wu, S. and Wu, Y.: 2009, The Spitzer Local Volume Legacy: Survey Description and Infrared Photometry, *ApJ* **703**, 517–556.
- de Blok, W. J. G., Walter, F., Brinks, E., Trachternach, C., Oh, S. and Kennicutt, R. C.: 2008, High-Resolution Rotation Curves and Galaxy Mass Models from THINGS, *AJ* **136**, 2648–2719.
- Drozdosky, I. O. and Karachentsev, I. D.: 2000, Photometric distances to six bright resolved galaxies, *A&AS* **142**, 425–432.
- Elmegreen, B. G., Palouš, J. and Ehlerova, S.: 2002, Environmental dependences for star formation triggered by expanding shell collapse, *MNRAS* **334**, 693–698.
- Engelbracht, C. W., Blaylock, M., Su, K. Y. L., Rho, J., Rieke, G. H., Muzerolle, J., Padgett, D. L., Hines, D. C., Gordon, K. D., Fadda, D., Noriega-Crespo, A., Kelly, D. M., Latter, W. B., Hinz, J. L., Misselt, K. A., Morrison, J. E., Stansberry, J. A., Shupe, D. L., Stolovy, S., Wheaton, W. A., Young, E. T., Neugebauer, G., Wachter, S., Perez-Gonzalez, P. G., Frayer, D. T. and Marleau, F. R.: 2007, Absolute Calibration and Characterization of the Multiband Imaging Photometer for Spitzer. I. The Stellar Calibrator Sample and the 24  $\mu\text{m}$  Calibration, *PASP* **119**, 994–1018.
- Eskridge, P. B., Frogel, J. A., Pogge, R. W., Quillen, A. C., Davies, R. L., DePoy, D. L., Houdashelt, M. L., Kuchinski, L. E., Ramirez, S. V., Sellgren, K., Terndrup, D. M. and Tiede, G. P.: 2000, The Frequency of Barred Spiral Galaxies in the Near-Infrared, *AJ* **119**, 536–544.
- Fazio, G. G., Hora, J. L., Allen, L. E., Ashby, M. L. N., Barmby, P., Deutsch, L. K., Huang, J., Kleiner, S., Marengo, M., Megeath, S. T., Melnick, G. J., Pahre, M. A., Patten, B. M., Polizotti, J., Smith, H. A., Taylor, R. S., Wang, Z., Willner, S. P., Hoffmann, W. F., Pipher, J. L., Forrest, W. J., McMurty, C. W., McCreight, C. R., McKelvey, M. E., McMurray, R. E., Koch, D. G., Moseley, S. H., Arendt, R. G., Mentzell, J. E., Marx, C. T., Losch, P., Mayman, P., Eichhorn, W., Krebs, D., Jhabvala, M.,

- Gezari, D. Y., Fixsen, D. J., Flores, J., Shakoorzadeh, K., Jungo, R., Hakun, C., Workman, L., Karpati, G., Kichak, R., Whitley, R., Mann, S., Tollestrup, E. V., Eisenhardt, P., Stern, D., Gorjian, V., Bhattacharya, B., Carey, S., Nelson, B. O., Glaccum, W. J., Lacy, M., Lowrance, P. J., Laine, S., Reach, W. T., Stauffer, J. A., Surace, J. A., Wilson, G., Wright, E. L., Hoffman, A., Domingo, G. and Cohen, M.: 2004, The Infrared Array Camera (IRAC) for the Spitzer Space Telescope, *ApJS* **154**, 10–17.
- Gonzalez Delgado, R. M. and Perez, E.: 1997, H II Region Population in a Sample of Nearby Galaxies with Nuclear Activity. II. Luminosity Function, Size, and Radial Distributions, *ApJS* **108**, 199–+.
- Gordon, K. D., Engelbracht, C. W., Rieke, G. H., Misselt, K. A., Smith, J.-D. T. and Kennicutt, Jr., R. C.: 2008, The Behavior of the Aromatic Features in M101 H II Regions: Evidence for Dust Processing, *ApJ* **682**, 336–354.
- Gordon, K. D., Rieke, G. H., Engelbracht, C. W., Muzerolle, J., Stansberry, J. A., Misselt, K. A., Morrison, J. E., Cadien, J., Young, E. T., Dole, H., Kelly, D. M., Alonso-Herrero, A., Egami, E., Su, K. Y. L., Papovich, C., Smith, P. S., Hines, D. C., Rieke, M. J., Blaylock, M., Pérez-González, P. G., Le Floc'h, E., Hinz, J. L., Latter, W. B., Hesselroth, T., Frayer, D. T., Noriega-Crespo, A., Masci, F. J., Padgett, D. L., Smylie, M. P. and Haegel, N. M.: 2005, Reduction Algorithms for the Multiband Imaging Photometer for Spitzer, *PASP* **117**, 503–525.
- Helfer, T. T., Thornley, M. D., Regan, M. W., Wong, T., Sheth, K., Vogel, S. N., Blitz, L. and Bock, D. C.-J.: 2003, The BIMA Survey of Nearby Galaxies (BIMA SONG). II. The CO Data, *ApJS* **145**, 259–327.
- Hernandez, O., Carignan, C., Amram, P., Chemin, L. and Daigle, O.: 2005, BH $\alpha$ BAR: big H $\alpha$  kinematical sample of barred spiral galaxies - I. Fabry-Perot observations of 21 galaxies, *MNRAS* **360**, 1201–1230.
- Hernández-Toledo, H. M., Zendejas-Domínguez, J. and Avila-Reese, V.: 2007, BVRI Surface Photometry of Isolated Spiral Galaxies, *AJ* **134**, 2286–2307.
- Hibbard, J. E., Bianchi, L., Thilker, D. A., Rich, R. M., Schiminovich, D., Xu, C. K., Neff, S. G., Seibert, M., Lauger, S., Burgarella, D., Barlow, T. A., Byun, Y., Donas, J., Forster, K., Friedman, P. G., Heckman, T. M., Jelinsky, P. N., Lee, Y., Madore, B. F., Malina, R. F., Martin, D. C., Milliard, B., Morrissey, P., Siegmund, O. H. W., Small, T., Szalay, A. S., Welsh, B. Y. and Wyder, T. K.: 2005, Ultraviolet Morphology and Star Formation in the Tidal Tails of NGC 4038/39, *ApJ* **619**, L87–L90.
- Iglesias-Páramo, J., Buat, V., Takeuchi, T. T., Xu, K., Boissier, S., Boselli, A., Burgarella, D., Madore, B. F., Gil de Paz, A., Bianchi, L., Barlow, T. A., Byun, Y., Donas, J., Forster, K., Friedman, P. G., Heckman, T. M., Jelinski, P. N., Lee, Y., Malina, R. F., Martin, D. C., Milliard, B., Morrissey, P. F., Neff, S. G., Rich, R. M., Schiminovich, D., Seibert, M., Siegmund, O. H. W., Small, T., Szalay, A. S., Welsh, B. Y. and Wyder, T. K.: 2006, Star Formation in the Nearby Universe: The Ultraviolet and Infrared Points of View, *ApJS* **164**, 38–51.

- Irwin, J. A., Hoffman, G. L., Spekkens, K., Haynes, M. P., Giovanelli, R., Linder, S. M., Catinella, B., Momjian, E., Koribalski, B. S., Davies, J., Brinks, E., de Blok, W. J. G., Putman, M. E. and van Driel, W.: 2009,  $\Lambda$ CDM Satellites and H I Companions - the Arecibo ALFA Survey of NGC 2903, *ApJ* **692**, 1447–1463.
- Jiang, I. and Binney, J.: 1999, WARPS and cosmic infall, *MNRAS* **303**, L7–L10.
- Jogee, S., Knapen, J. H., Laine, S., Shlosman, I., Scoville, N. Z. and Englmaier, P.: 2002, Discovery and Implications of a New Large-Scale Stellar Bar in NGC 5248, *ApJ* **570**, L55–L59.
- Kamphuis, J. J., Sijbring, D. and van Albada, T. S.: 1996, Global H I profiles of spiral galaxies., *A&AS* **116**, 15–20.
- Karachentseva, V. E.: 1973, Catalogue of isolated galaxies., *Soobshcheniya Spetsial'noj Astrofizicheskoy Observatorii* **8**, 3–+.
- Kennicutt, Jr., R. C.: 1983, The rate of star formation in normal disk galaxies, *ApJ* **272**, 54–67.
- Kennicutt, Jr., R. C.: 1998, Star Formation in Galaxies Along the Hubble Sequence, *ARA&A* **36**, 189–232.
- Kennicutt, Jr., R. C., Armus, L., Bendo, G., Calzetti, D., Dale, D. A., Draine, B. T., Engelbracht, C. W., Gordon, K. D., Grauer, A. D., Helou, G., Hollenbach, D. J., Jarrett, T. H., Kewley, L. J., Leitherer, C., Li, A., Malhotra, S., Regan, M. W., Rieke, G. H., Rieke, M. J., Roussel, H., Smith, J., Thornley, M. D. and Walter, F.: 2003, SINGS: The SIRTf Nearby Galaxies Survey, *PASP* **115**, 928–952.
- Kennicutt, Jr., R. C., Calzetti, D., Walter, F., Helou, G., Hollenbach, D. J., Armus, L., Bendo, G., Dale, D. A., Draine, B. T., Engelbracht, C. W., Gordon, K. D., Prescott, M. K. M., Regan, M. W., Thornley, M. D., Bot, C., Brinks, E., de Blok, E., de Mello, D., Meyer, M., Moustakas, J., Murphy, E. J., Sheth, K. and Smith, J. D. T.: 2007, Star Formation in NGC 5194 (M51a). II. The Spatially Resolved Star Formation Law, *ApJ* **671**, 333–348.
- Kennicutt, Jr., R. C., Edgar, B. K. and Hodge, P. W.: 1989, Properties of H II region populations in galaxies. II - The H II region luminosity function, *ApJ* **337**, 761–781.
- Kennicutt, Jr., R. C. and Kent, S. M.: 1983, A survey of H-alpha emission in normal galaxies, *AJ* **88**, 1094–1107.
- Kennicutt, R. C., Hao, C., Calzetti, D., Moustakas, J., Dale, D. A., Bendo, G., Engelbracht, C. W., Johnson, B. D. and Lee, J. C.: 2009, Dust-corrected Star Formation Rates of Galaxies. I. Combinations of H $\alpha$  and Infrared Tracers, *ApJ* **703**, 1672–1695.
- Knapen, J. H., Shlosman, I. and Peletier, R. F.: 2000, A Subarcsecond Resolution Near-Infrared Study of Seyfert and “Normal” Galaxies. II. Morphology, *ApJ* **529**, 93–100.
- Kong, X., Charlot, S., Brinchmann, J. and Fall, S. M.: 2004, Star formation history and dust content of galaxies drawn from ultraviolet surveys, *MNRAS* **349**, 769–778.
- Koribalski, B. S. and López-Sánchez, Á. R.: 2009, Gas dynamics and star formation in the galaxy pair NGC1512/1510, *MNRAS* **400**, 1749–1767.

- Kormendy, J.: 1979, A morphological survey of bar, lens, and ring components in galaxies Secular evolution in galaxy structure, *ApJ* **227**, 714–728.
- Kuchinski, L. E., Freedman, W. L., Madore, B. F., Trewhella, M., Bohlin, R. C., Cornett, R. H., Fanelli, M. N., Marcum, P. M., Neff, S. G., O’Connell, R. W., Roberts, M. S., Smith, A. M., Stecher, T. P. and Waller, W. H.: 2000, Comparing Galaxy Morphology at Ultraviolet and Optical Wavelengths, *ApJS* **131**, 441–463.
- Laurikainen, E. and Salo, H.: 2002, Bar strengths in spiral galaxies estimated from 2MASS images, *MNRAS* **337**, 1118–1138.
- Lee, J. C., Gil de Paz, A., Tremonti, C., Kennicutt, R. C., Salim, S., Bothwell, M., Calzetti, D., Dalcanton, J., Dale, D., Engelbracht, C., Funes, S. J. J. G., Johnson, B., Sakai, S., Skillman, E., van Zee, L., Walter, F. and Weisz, D.: 2009, Comparison of H $\alpha$  and UV Star Formation Rates in the Local Volume: Systematic Discrepancies for Dwarf Galaxies, *ApJ* **706**, 599–613.
- Lee, J. C., Kennicutt, R. C., Engelbracht, C. W., Calzetti, D., Dale, D. A., Gordon, K. D., Dalcanton, J. J., Skillman, E., Begum, A., Funes, J. G., Gil de Paz, A., Johnson, B., Sakai, S., van Zee, L., Walter, F., Weisz, D., Williams, B., Wu, Y. and Block, M.: 2008, The Local Volume Legacy Survey, in J. G. Funes & E. M. Corsini (ed.), *Astronomical Society of the Pacific Conference Series*, Vol. 396 of *Astronomical Society of the Pacific Conference Series*, pp. 151–+.
- Leitherer, C., Schaerer, D., Goldader, J. D., González Delgado, R. M., Robert, C., Kune, D. F., de Mello, D. F., Devost, D. and Heckman, T. M.: 1999, Starburst99: Synthesis Models for Galaxies with Active Star Formation, *ApJS* **123**, 3–40.
- Leon, S., Jeyakumar, S., Pérez-Ramírez, D., Verdes-Montenegro, L., Lee, S. W. and Ocaña Flaquer, B.: 2008, HCN(1-0) enhancement in the bar of NGC 2903, *A&A* **491**, 703–711.
- Marinova, I. and Jogee, S.: 2007, Characterizing Bars at  $z \sim 0$  in the Optical and NIR: Implications for the Evolution of Barred Disks with Redshift, *ApJ* **659**, 1176–1197.
- Martin, D. C., Fanson, J., Schiminovich, D., Morrissey, P., Friedman, P. G., Barlow, T. A., Conrow, T., Grange, R., Jelinsky, P. N., Milliard, B., Siegmund, O. H. W., Bianchi, L., Byun, Y.-I., Donas, J., Forster, K., Heckman, T. M., Lee, Y.-W., Madore, B. F., Malina, R. F., Neff, S. G., Rich, R. M., Small, T., Surber, F., Szalay, A. S., Welsh, B. and Wyder, T. K.: 2005, The Galaxy Evolution Explorer: A Space Ultraviolet Survey Mission, *ApJ* **619**, L1–L6.
- Martin, P. and Friedli, D.: 1997, Star formation in bar environments. I. Morphology, star formation rates and general properties., *A&A* **326**, 449–464.
- Mayya, Y. D.: 1994, Embedded clusters in giant extragalactic H II regions, 1: BVRH-alpha photometry, *AJ* **108**, 1276–1291.
- Menéndez-Delmestre, K., Sheth, K., Schinnerer, E., Jarrett, T. H. and Scoville, N. Z.: 2007, A Near-Infrared Study of 2MASS Bars in Local Galaxies: An Anchor for High-Redshift Studies, *ApJ* **657**, 790–804.

- Ostriker, E. C. and Binney, J. J.: 1989, Warped and tilted galactic discs, *MNRAS* **237**, 785–798.
- Pence, W. D. and Blackman, C. P.: 1984, Dynamics of gas in barred spiral galaxies. I - NGC 6221, *MNRAS* **207**, 9–23.
- Pérez-González, P. G., Kennicutt, Jr., R. C., Gordon, K. D., Misselt, K. A., Gil de Paz, A., Engelbracht, C. W., Rieke, G. H., Bendo, G. J., Bianchi, L., Boissier, S., Calzetti, D., Dale, D. A., Draine, B. T., Jarrett, T. H., Hollenbach, D. and Prescott, M. K. M.: 2006, Ultraviolet through Far-Infrared Spatially Resolved Analysis of the Recent Star Formation in M81 (NGC 3031), *ApJ* **648**, 987–1006.
- Pérez, I., Fux, R. and Freeman, K.: 2004, Gas flow and dark matter in the inner parts of early-type barred galaxies. I. SPH simulations and comparison with the observed kinematics, *A&A* **424**, 799–815.
- Pilyugin, L. S., Vílchez, J. M. and Contini, T.: 2004, Oxygen and nitrogen abundances in nearby galaxies. Correlations between oxygen abundance and macroscopic properties, *A&A* **425**, 849–869.
- Popping, G., Perez, I. and Zurita, A.: 2010, Multiwavelength study of the star formation in the bar of NGC 2903, *ArXiv e-prints* .
- Regan, M. W., Thornley, M. D., Helfer, T. T., Sheth, K., Wong, T., Vogel, S. N., Blitz, L. and Bock, D. C.-J.: 2001, The BIMA Survey of Nearby Galaxies. I. The Radial Distribution of CO Emission in Spiral Galaxies, *ApJ* **561**, 218–237.
- Relaño, M., Beckman, J. E., Zurita, A., Rozas, M. and Giammanco, C.: 2005, The internal dynamical equilibrium of H II regions: A statistical study, *A&A* **431**, 235–251.
- Relaño, M. and Kennicutt, R. C.: 2009, Star Formation in Luminous H II Regions in M33, *ApJ* **699**, 1125–1143.
- Reynaud, D. and Downes, D.: 1998, Kinematics of the gas in a barred galaxy: do strong shocks inhibit star formation?, *A&A* **337**, 671–680.
- Rieke, G. H., Young, E. T., Engelbracht, C. W., Kelly, D. M., Low, F. J., Haller, E. E., Beeman, J. W., Gordon, K. D., Stansberry, J. A., Misselt, K. A., Cadien, J., Morrison, J. E., Rivlis, G., Latter, W. B., Noriega-Crespo, A., Padgett, D. L., Stapelfeldt, K. R., Hines, D. C., Egami, E., Muzerolle, J., Alonso-Herrero, A., Blaylock, M., Dole, H., Hinz, J. L., Le Floch, E., Papovich, C., Pérez-González, P. G., Smith, P. S., Su, K. Y. L., Bennett, L., Frayer, D. T., Henderson, D., Lu, N., Masci, F., Pesenson, M., Rebull, L., Rho, J., Keene, J., Stolovy, S., Wachter, S., Wheaton, W., Werner, M. W. and Richards, P. L.: 2004, The Multiband Imaging Photometer for Spitzer (MIPS), *ApJS* **154**, 25–29.
- Rozas, M., Zurita, A., Heller, C. H. and Beckman, J. E.: 1999, Global properties of the population of HII regions in NGC 7479 from photometric H $\alpha$  imaging, *A&AS* **135**, 145–158.
- Salim, S., Rich, R. M., Charlot, S., Brinchmann, J., Johnson, B. D., Schiminovich, D., Seibert, M., Mallery, R., Heckman, T. M., Forster, K., Friedman, P. G., Martin, D. C., Morrissey, P., Neff, S. G., Small, T., Wyder, T. K., Bianchi, L., Donas, J., Lee, Y., Madore, B. F., Milliard, B., Szalay, A. S., Welsh, B. Y. and Yi, S. K.: 2007, UV Star Formation Rates in the Local Universe, *ApJS* **173**, 267–292.

- Sancisi, R., Fraternali, F., Oosterloo, T. and van der Hulst, T.: 2008, Cold gas accretion in galaxies, *A&A Rev.* **15**, 189–223.
- Schlegel, D. J., Finkbeiner, D. P. and Davis, M.: 1998, Maps of Dust Infrared Emission for Use in Estimation of Reddening and Cosmic Microwave Background Radiation Foregrounds, *ApJ* **500**, 525–+.
- Scoville, N. Z., Polletta, M., Ewald, S., Stolovy, S. R., Thompson, R. and Rieke, M.: 2001, High-Mass, OB Star Formation in M51: Hubble Space Telescope H $\alpha$  and Pa $\alpha$  Imaging, *AJ* **122**, 3017–3045.
- Sellwood, J. A. and Sánchez, R. Z.: 2010, Quantifying non-circular streaming motions in disc galaxies, *MNRAS* **404**, 1733–1744.
- Sheth, K., Regan, M. W., Vogel, S. N. and Teuben, P. J.: 2000, Molecular Gas, Dust, and Star Formation in the Barred Spiral NGC 5383, *ApJ* **532**, 221–237.
- Sheth, K., Vogel, S. N., Regan, M. W., Teuben, P. J., Harris, A. I. and Thornley, M. D.: 2002, Molecular Gas and Star Formation in Bars of Nearby Spiral Galaxies, *AJ* **124**, 2581–2599.
- Shlosman, I., Frank, J. and Begelman, M. C.: 1989, Bars within bars - A mechanism for fuelling active galactic nuclei, *Nature* **338**, 45–47.
- Springob, C. M., Haynes, M. P., Giovanelli, R. and Kent, B. R.: 2005, A Digital Archive of H I 21 Centimeter Line Spectra of Optically Targeted Galaxies, *ApJS* **160**, 149–162.
- Tamura, K., Jansen, R. A. and Windhorst, R. A.: 2009, Mapping the Spatial Distribution of Dust Extinction in NGC 959 Using Broadband Visible and Mid-Infrared Filters, *AJ* **138**, 1634–1654.
- Thilker, D. A., Bianchi, L., Boissier, S., Gil de Paz, A., Madore, B. F., Martin, D. C., Meurer, G. R., Neff, S. G., Rich, R. M., Schiminovich, D., Seibert, M., Wyder, T. K., Barlow, T. A., Byun, Y., Donas, J., Forster, K., Friedman, P. G., Heckman, T. M., Jelinsky, P. N., Lee, Y., Malina, R. F., Milliard, B., Morrissey, P., Siegmund, O. H. W., Small, T., Szalay, A. S. and Welsh, B. Y.: 2005, Recent Star Formation in the Extreme Outer Disk of M83, *ApJ* **619**, L79–L82.
- Thilker, D. A., Boissier, S., Bianchi, L., Calzetti, D., Boselli, A., Dale, D. A., Seibert, M., Braun, R., Burgarella, D., Gil de Paz, A., Helou, G., Walter, F., Kennicutt, Jr., R. C., Madore, B. F., Martin, D. C., Barlow, T. A., Forster, K., Friedman, P. G., Morrissey, P., Neff, S. G., Schiminovich, D., Small, T., Wyder, T. K., Donas, J., Heckman, T. M., Lee, Y., Milliard, B., Rich, R. M., Szalay, A. S., Welsh, B. Y. and Yi, S. K.: 2007, Ultraviolet and Infrared Diagnostics of Star Formation and Dust in NGC 7331, *ApJS* **173**, 572–596.
- Trachternach, C., de Blok, W. J. G., Walter, F., Brinks, E. and Kennicutt, R. C.: 2008, Dynamical Centers and Noncircular Motions in THINGS Galaxies: Implications for Dark Matter Halos, *AJ* **136**, 2720–2760.
- van der Hulst, J. M., Terlouw, J. P., Begeman, K. G., Zwitser, W. and Roelfsema, P. R.: 1992, The Groningen Image Processing SYstem, GIPSY, in D. M. Worrall, C. Biemesderfer, & J. Barnes (ed.), *Astronomical Data Analysis Software and Systems I*, Vol. 25 of *Astronomical Society of the Pacific Conference Series*, pp. 131–+.

- van der Hulst, J. M., van Albada, T. S. and Sancisi, R.: 2001, The Westerbork HI Survey of Irregular and Spiral Galaxies, WHISP, in J. E. Hibbard, M. Rupen, & J. H. van Gorkom (ed.), *Gas and Galaxy Evolution*, Vol. 240 of *Astronomical Society of the Pacific Conference Series*, pp. 451–+.
- Verley, S., Corbelli, E., Giovanardi, C. and Hunt, L. K.: 2009, Star formation in M 33: multiwavelength signatures across the disk, *A&A* **493**, 453–466.
- Vogelaar, M. G. R. and Terlouw, J. P.: 2001, The Evolution of GIPSY—or the Survival of an Image Processing System, in F. R. Harnden Jr., F. A. Primini, & H. E. Payne (ed.), *Astronomical Data Analysis Software and Systems X*, Vol. 238 of *Astronomical Society of the Pacific Conference Series*, pp. 358–+.
- van Hoppel, T. and Bothun, G.: 1990, The luminosities of bright H II regions in NGC 628 and its O star formation rate, *AJ* **100**, 403–414.
- Werner, M. W., Roellig, T. L., Low, F. J., Rieke, G. H., Rieke, M., Hoffmann, W. F., Young, E., Houck, J. R., Brandl, B., Fazio, G. G., Hora, J. L., Gehrz, R. D., Helou, G., Soifer, B. T., Stauffer, J., Keene, J., Eisenhardt, P., Gallagher, D., Gautier, T. N., Irace, W., Lawrence, C. R., Simmons, L., Van Cleve, J. E., Jura, M., Wright, E. L. and Cruikshank, D. P.: 2004, The Spitzer Space Telescope Mission, *ApJS* **154**, 1–9.
- Wong, O. I., Ryan-Weber, E. V., Garcia-Appadoo, D. A., Webster, R. L., Staveley-Smith, L., Zwaan, M. A., Meyer, M. J., Barnes, D. G., Kilborn, V. A., Bhathal, R., de Blok, W. J. G., Disney, M. J., Doyle, M. T., Drinkwater, M. J., Ekers, R. D., Freeman, K. C., Gibson, B. K., Gurovich, S., Harnett, J., Henning, P. A., Jerjen, H., Kesteven, M. J., Knezek, P. M., Koribalski, B. S., Mader, S., Marquarding, M., Minchin, R. F., O’Brien, J., Putman, M. E., Ryder, S. D., Sadler, E. M., Stevens, J., Stewart, I. M., Stootman, F. and Waugh, M.: 2006, The Northern HIPASS catalogue - data presentation, completeness and reliability measures, *MNRAS* **371**, 1855–1864.
- Zurita, A. and Pérez, I.: 2008, Where are the stars of the bar of NGC 1530 forming?, *A&A* **485**, 5–20.
- Zurita, A., Relaño, M., Beckman, J. E. and Knapen, J. H.: 2004, Ionized gas kinematics and massive star formation in NGC 1530, *A&A* **413**, 73–89.